Austrian Journal of Earth Sciences | Vienna | 2024 | Volume 117 | 87–112 | DOI: 10.17738/ajes.2024.0007

Polymetallic tungsten skarn mineralisation related to the Periadriatic intrusion at Lienzer Schlossberg, East Tyrol, Austria

Johann G. Raith[1]*, Florian Hutter[1,5], Florian Altenberger[1], Julia Weilbold[2], Christian Auer[2], Joachim Krause[3], Jasper Berndt[4], Hassan Neinavaie[6]

[1)] Chair of Resource Mineralogy, Montanuniversität Leoben, Peter Tunner-Straße 5, 8700 Leoben, Austria; johann.raith@unileoben.ac.at, ORCID: 0000-0002-4546-2319; florian.altenberger@unileoben.ac.at, ORCID: 0009-0000-7179-8492;

[2)] GeoSphere Austria, Hohe Warte 38, 1190 Vienna, Austria; christian.auer@geosphere.at; julia.weilbold@geosphere.at;

[3)] Helmholtz-Zentrum Dresden-Rossendorf, Helmholtz Institute Freiberg for Resource Technology, Chemnitzer Straße 40, 09599 Freiberg, Germany; joachim.krause@hzdr.de, ORCID: 0000-0001-8552-3318;

[4)] Institute for Mineralogy, University of Münster, Corrensstraße 24, 48149 Münster, Germany; jberndt@uni-muenster.de;

[5)] geo.zt gmbh – poscher beratende geologen, Saline 17, 6060 Hall in Tirol; fhutter3@gmail.com

[6)] Rennfeld 28, 6370 Kitzbühel, Austria

[*)] Corresponding author: johann.raith@unileoben.ac.at

Keywords: Eastern Alps, scheelite, tungsten skarn, Periadriatic intrusion, trace elements, LA-ICP-MS

Abstract

A regional tungsten anomaly was discovered and explored in the Lienzer Schlossberg area that is part of the crystalline Austroalpine nappe complex of the Eastern Alps in the 1970/80-ties. Tungsten is present as scheelite, which occurs in steeply SSW dipping WNW-ENE oriented quartz veinlets and joints within the porphyritic dioritic to tonalitic/granodioritic host rocks of the Oligocene Lienz/Edenwald intrusion and in the exoskarn, which developed at the contact of the intrusion with Ca-rich lithologies. The skarn system is characterised by two stages: (1) a primary high-temperature calc-silicate stage characterised by grossular, diopside-hedenbergite, vesuvianite, wollastonite and Ca-plagioclase and (2) a retrograde skarn stage including scheelite-bearing massive sulphide ores (pyrrhotite, chalcopyrite, tremolite-actinolite, diopside-hedenbergite) and scheelite-rich fault rocks with calcite, sericite and chlorite. The two ore stages, the mineral paragenesis and composition is like that of a reduced tungsten skarn; i.e., garnet is grossular-rich, clinopyroxene is diopside-hedenbergite. Vesuvianite contains up to 1.8 mass % fluorine. Scheelite has been studied by cathodoluminescence (CL), electron probe microanalysis and laser ablation-inductively coupled plasma-mass spectrometry. Three types of scheelite (Scheelite 1–3) are distinguished. In short-wave UV light, all types show blue fluorescence but CL revealed internal micro-textures in scheelite grains which are dominated by oscillatory zoning. Prolonged hydrothermal activity is indicated by dissolution-replacement and overgrowth textures affecting the primary zonation and trace element composition of scheelite. The distribution of rare earth elements (REE) in Scheelite 1 in tonalite-hosted quartz veinlets shows a convex (i.e., middle REE-enriched), heavy REE-depleted pattern with negative Eu anomalies (Eu_A). The evolution of REE patterns from skarn-hosted Scheelite 2 and 3 illustrates a gradation of convex REE patterns with high ΣREE and distinct negative Eu anomalies to relatively flat REE patterns with small to no Eu_A. Scheelite at Lienzer Schlossberg has one of the highest ΣREE+Y contents of all scheelite-bearing ore settings in the Eastern Alps but incorporates minor Mo and the least Sr. High Na and Nb contents together with the positive correlation of REE+Y vs. Na+Nb+Ta suggests that the main exchange vectors for REE incorporation in scheelite is via a combined coupled substitution mechanism. Results of this study confirm the genetic similarity with reduced tungsten skarns and highlight the tungsten potential of this area.

1. Introduction

In the Eastern Alps, dozens of subeconomic scheelite ($CaWO_4$) showings are known (Weber and Lipiarski, 2020) making them one of the orogenic belts with high tungsten endowment (Fig. 1). Most have been classified as strata-bound scheelite deposits without any obvious association with igneous intrusive rocks (Höll, 1979; Altenberger et al., 2021). Tungsten mineralisation in the Eastern Alps represents different mineralisation styles. Among these, Felbertal is a unique tungsten deposit of global economic importance (for a review see Raith et al., 2018).

The majority of global tungsten deposits are of magmatic-hydrothermal origin with clear spatial and genetic links to felsic plutons (Schmidt, 2012). The most important tungsten producers are skarn deposits representing the world's major resources of tungsten (Green et al., 2020). Skarns are metasomatic rocks composed of calc-silicate minerals. They are of different origins and form by interaction of various lithologies, commonly containing some limestone, with fluids of magmatic, metamorphic, meteoric and/or marine origin (Meinert, 1992). The most important group are magmatogenic skarn deposits where the magmatic-hydrothermal fluids derived from a nearby crystallising felsic pluton. In addition to W, a variety of commodities like Fe, Mo, Au, Cu and Zn were mined from such pluton-related skarn deposits (Einaudi et al., 1981; Meinert, 1992).

Tungsten skarns are typically associated with calc-alkalic plutons, which are surrounded by large contact metamorphic aureoles with abundant pelitic hornfelses and calc-silicate fels. Commonly, they are calcic skarns that form at rather deeper crustal levels (200–300 MPa) (Meinert, 1992). Prograde and retrograde skarn stages are commonly recorded. An early stage of isochemical contact metamorphism with possible formation of local reaction skarns is followed by the main prograde skarn stage. It is characterised by infiltration of hot magmatic-hydrothermal fluids, which react with the host rocks to form endoskarn and exoskarn zones. In the latter the typical anhydrous calc-silicate minerals are clinopyroxene, calcic garnet, wollastonite, vesuvianite and Mo-bearing scheelite. A regional zonation (garnet-pyroxene-wollastonite) away from the contact can be developed. Temperatures up to about 600–700 °C are recorded for this stage in tungsten skarns (Newberry and Einaudi, 1981; Meinert, 1992). During cooling of the system, retrograde skarn assemblages form in a temperature range of about 300–400 °C. Especially in shallow skarn systems they overprint the high-temperature minerals and develop along late structural zones and in veins. Hydrous silicates like calcic amphiboles and epidote are characteristic minerals. Sulphides (pyrrhotite, molybdenite, chalcopyrite, sphalerite, arsenopyrite) are commonly associated with the retrograde stage of tungsten skarns (Sánchez et al., 2009; Poitrenaud et al., 2019).

Based on the redox conditions during ore formation, tungsten skarns have been classified as reduced or oxidised (Einaudi et al., 1981; Miranda et al., 2022). The economically more important reduced type is characterised by predominance of ferrous over ferric iron. Mineralogically, this is reflected by the predominance of hedenbergite that coexists with grossular garnet. In contrast, oxidised tungsten skarns have diopside plus andradite garnet. In the sulphide assemblages of the retrograde stage, the rather reduced nature of tungsten skarns is indicated by the predominance of pyrrhotite over pyrite. Scheelite of the retrograde stage is Mo-poor (Miranda et al., 2022).

Though Palaeozoic intrusive rocks are widespread in the Alpine basements (von Raumer et al., 2013), true magmatogenic skarn deposits seem, however, to be rare in the Eastern Alps. This might primarily be caused by the scarcity of intrusive rocks of Cenozoic age found in the Alpine orogen, which are restricted to the Periadriatic Fault System, a crustal-scale fault system separating the Eastern Alps from the Southern Alps (Fig. 1). An exception might be the intrusion at Lienzer Schlossberg area situated in the crystalline Austroalpine nappe complex of the Eastern Alps. There, a regional tungsten anomaly with several scheelite showings has been discovered during tungsten exploration in the late 1970-ties to early 1980-ties (Voest-Alpine AG, 1979; Neinavaie et al., 1983; Raith, 1983).

Considering the general economic importance of tungsten skarns, it is not only of scientific interest to investigate these scheelite showings in more detail. This paper therefore describes the different types of tungsten mineralisation in the study area with a focus on the skarns. It reports mineralogical data of ores from historic mine workings and skarn assemblages which developed in the contact metamorphic aureole around the Oligocene Edenwald intrusion. Moreover, we present and discuss the micro-textures and trace element characteristics of scheelite. We aim to show that the polymetallic skarn and vein-type scheelite mineralisation in this area is part of a magmatic-hydrothermal system related to this intrusion. It is the best example of a tungsten bearing skarn system known from the Eastern Alps.

2. Geologial setting and mineralisation

2.1. Thurntaler Complex

The Thurntaler Complex is part of the Gondwana-derived Austroalpine basement complexes to the south of the Tauern Window, which record a complex Neoproterozoic to early Paleozoic geodynamic evolution (Schulz et al., 2004). It is assigned to the Upper Austroalpine Drauzug-Gurktal Nappe System (Schmid et al., 2004; Linner et al., 2013). In older literature it is also referred to as "Thurntaler Quarzphyllit" (Furlani, 1912; Senarclens-Grancy, 1965; Heinisch and Schmidt, 1984), one of the several low-grade metamorphic Paleozoic quartzphyllite units in the Eastern Alps (Neubauer and Sassi, 1993). The Thurntaler Complex stretches north of the Pustertal valley from

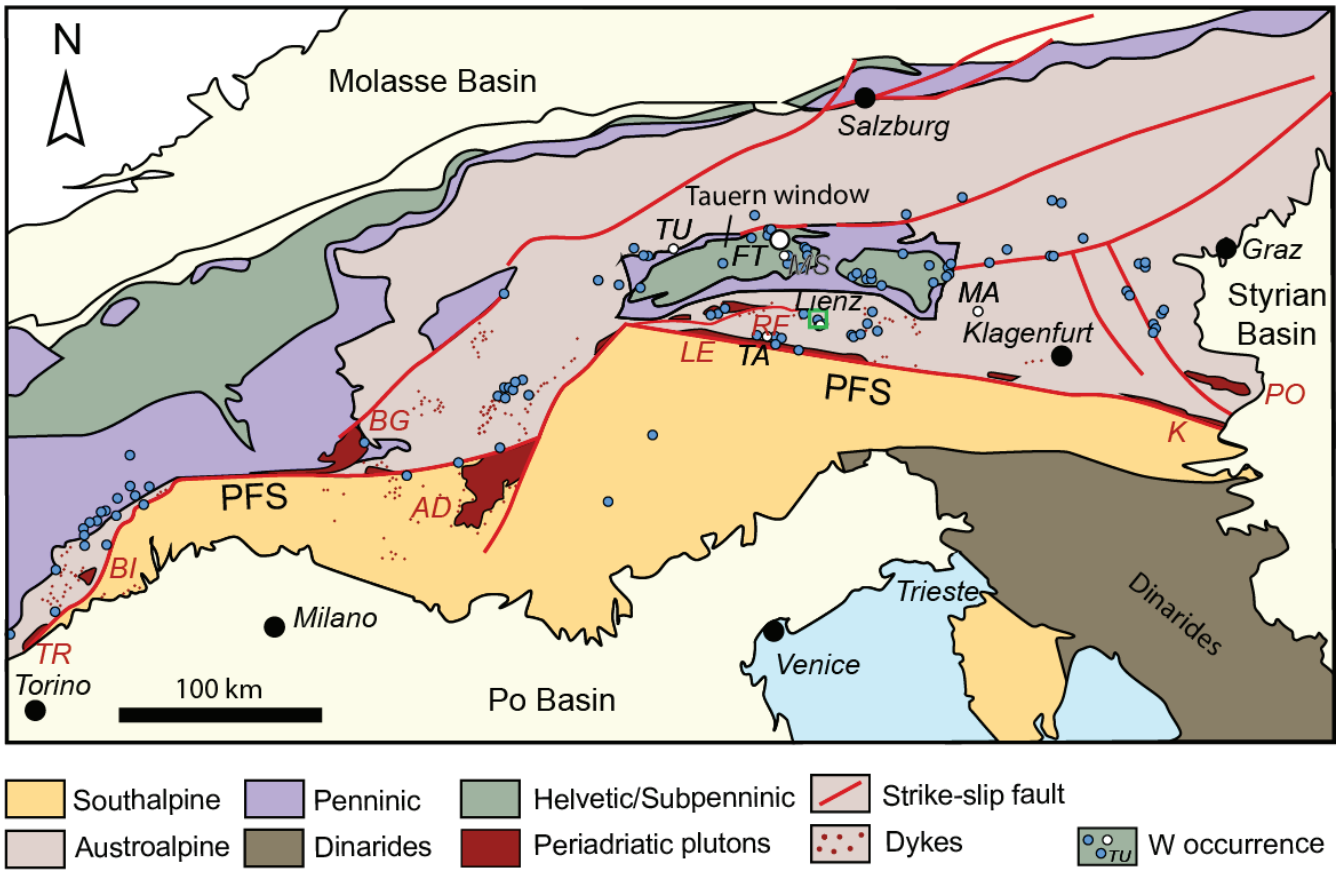

Figure 1: Simplified geological map of the Alps showing the major units and the distribution of Periadriatic plutons and dykes (modified, after Neubauer et al., 2018). Study area near Lienz is shown as green rectangle (see Fig. 2). PFS = Periadriatic Fault System, Periadriatic plutons: PO = Pohorje, K = Karawanken, LE = Lesachtal, RF = Rieserferner, AD = Adamello, BG = Bergell, BI = Biella, TR = Traversella. Tungsten occurrences (blue and white filled circles) are also shown; FT = Felbertal tungsten mine, MA = Mallnock, MS = Messelingscharte, TA = Tafinalpe, TU = Tux-Lanersbach (sources are Altenberger et al., 2021; Brigo and Omenetto, 1983).

Toblach to Lienz and it is tectonically separated from the higher grade metamorphic Defereggen Complex. It overlies the Defereggen Complex along a partly overturned pre-Alpine foliation-parallel contact represented by a several hundreds of meters wide mylonite zone (Furlani, 1912; Heinisch and Schmidt, 1984; Schulz and Bombach, 2003; Schulz et al., 2004; Schulz et al., 2008).

The Thurntaler Complex consists of low to medium grade metapelites and metapsammites (quartzphyllite, phyllitic micaschist) with intercalations of felsic metavolcanics (metaporphyroid), metabasites (amphibolite, greenschist, hornblende prasinite) and minor graphitic schists, orthogneiss, and rare thin marble layers (Fig. 2, Heinisch and Schmidt, 1976; Heinisch and Schmidt, 1984; Schulz, 1991). The youngest detrital U-Pb zircon ages in metapsammopelites of the Thurntaler Complex are 551 ± 26 Ma and 576 ± 12 Ma (Siegesmund et al., 2018). Finely banded quartz-rich metaporphyroids become more abundant in the tectonic higher part of the sequence. The SiO_2-rich (67–79 mass % SiO_2) metaporphyroids, which are interpreted as metavolcanic rocks, yielded Lower/Middle Ordovician Pb-Pb single zircon ages falling in the range of 460–480 Ma; weighted mean ages of two samples are 473 ± 7 and 469 ± 6 Ma (Schulz et al., 2004). A SHRIMP U-Pb zircon age of 477 ± 4 Ma confirmed this data (Siegesmund et al., 2007). Granodioritic orthogneisses were dated at 434 ± 4 Ma (Borsi et al., 1973) but more recent age data show that their emplacement age strongly overlaps with the metaporphyroids. The SiO_2-rich rocks were interpreted as syn-collisional to late orogenic crustal melts formed during the amalgamation and collision of crustal terranes with the Gondwana margin in the Ordovician (Schulz et al., 2004; Schulz et al., 2008).

The metabasites (42–51 mass % SiO_2) have tholeiitic to alkaline chemical characteristics and derived from basalts of transitional mid-ocean ridge (MORB) and within plate (WPB) affinity (Schulz et al., 2006). The Pb-Pb zircon age of these metabasites is 432 ± 5.5 Ma (Schulz and Bombach, 2003). Formation of the protoliths is seen in context of the evolution of a Neoproterozoic to Cambrian active margin, opening of an "crypto-Rheic" ocean in the Lower Ordovician and subsequent subduction and collision in the Middle to Upper Ordovician (Schulz et al., 2004; Schulz et al., 2008).

Rocks from the Thurntaler Complex are polymetamorphic. Outside the contact metamorphic aureole, assemblages with garnet, biotite, chlorite, muscovite, oligoclase and quartz are observed in phyllitic micaschists,

lacking staurolite and aluminosilicates (Schulz, 1991; Linner, 2003). They are interlayered with quartzphyllite and contain dm-thick quartzite layers and vein quartz segregations. Maximum calculated temperature-pressure conditions of Variscan metamorphism are 560 °C/0.6 GPa (Schulz, 1991; Schulz, 1993). In the metabasites, relicts of hornblende and oligoclase confirm epidote-amphibolite facies metamorphism (Schulz, 1991; Schulz et al., 2004). Alpine regional metamorphism was low grade (<300 °C).

Three ductile deformation events have been distinguished in the Thurntaler Complex (Linner, 2003). Relict F1 folds are assigned to D1. The main penetrative S2 foliation and F2 folds are assigned to D2, which is the dominant deformation event. Juxtaposition of the Thurntaler Complex with metamorphic rocks of the Defereggen Complex and formation of the mylonite zone in between is also syn-D2 (Heinisch and Schmidt, 1976). D3 is evidenced by F3 folds on mm- to km-scale and various L3 lineations. It also resulted in large-scale folding and faulting (Guhl and Troll, 1987; Schulz and Bombach, 2003). D4 and D5 shear bands were recognised in phyllitic micaschists of the Defereggen Complex adjacent to the Thurntaler Complex (Schulz et al., 2008).

In the Edenwald area, the host rocks of the Oligocene intrusion are phyllonitic micaschists and schistose gneisses of the Thurntaler and Defereggen complexes with minor augengneiss intercalations (e.g., at Pfister quarry). Contact metamorphic hornfels dominates within the aureole (Fig. 2).

2.2. The Periadriaric Lienz/Edenwald intrusion

The Lienz/Edenwald intrusion extends from Pölland in the Isel valley towards south to Taxer Gassl and from there in NW-SE direction to Sternalm north of Leisach (Fig. 2). The intrusion is exposed over a length and width of ca. 3000 × 1000 m and a vertical distance of about 1000 m. The large vertical exposure suggests that the intrusion contact is steep. Regional mapping confirmed the intrusive nature of the Edenwald intrusion. The contact to the surrounding rocks of the Thurntaler Complex is discordant with an acute angle between the two units (Linner, 2003; Linner et al., 2013). Tonalitic dykes with porphyritic micro-structure are exposed along the southwestern to southern contact (Fig. 2) but are missing in the northeast, what may indicate a southwest plunging of the intrusion (Linner, 2003). Trails of mega-xenoliths of hornfels have been observed too; they could be roof pendants of contact metamorphosed host rocks.

The emplacement of the composite tonalite intrusion in the Middle Oligocene (30 Ma; Borsi et al., 1978) into these metamorphic rocks caused the formation of a 250–1000 m wide contact metamorphic aureole, which is best developed at the western to southern margin of the intrusion (Fig. 2; Linner, 2003; Linner et al., 2013). Various types of hornfels, from schistose to massive varieties, formed in this contact aureole. From the outer zone towards the intrusive contact schistose hornfels with muscovite + biotite + quartz + plagioclase ± andalusite grade into cordierite + sillimanite hornfels gneiss and locally migmatitic sillimanite-K-feldspar-bearing hornfels. Corundum and spinel are also present in the hornfels of the innermost contact metamorphic zone (Linner, 2003). Intercalations of thin marble and calc-silicate layers are rare but a key lithology for mineralisation.

2.3. Base metal mineralisation and tungsten prospecting

The area of interest at Lienzer Schlossberg is assigned to the polymetallic skarn district Lienz-Hochstein of the Drauzug-Gurktal Nappe System (Weber and Lipiarski, 2020). It is part of the Austroalpine nappe complex of the Eastern Alps (Schmid et al., 2004). Several historic mines and mineral showings containing pyrrhotite, arsenopyrite and base metal sulphides have been documented in this area (Fig. 2; Neinavaie et al., 1983; Exel, 1986), including:

1. Lienzer Schlossberg – Moosalm: open pit and dumps of a pyrrhotite-dominated massive sulphide mineralisation (Fuchs, 1982; Neinavaie, 1979; Neinavaie et al., 1983; Raith, 1983);
2. Hoferschacht: arsenopyrite, Fe-rich sphalerite, pyrite and galena in a silicified cataclasite, associated with Sn minerals (cassiterite, stannite) and various secondary Pb-minerals (Friedrich, 1949; Auer, 2016);
3. Edenwiese: prospect for pyrite, pyrrhotite, arsenopyrite, galena and sphalerite in a 20–30 cm thick quartz vein;
4. Wolfesbach: prospect targeting a pyrrhotite lens;
5. Hochsteinhütte: historic mining for arsenopyrite in quartz veins;
6. Taxer Gassl: up to 2 m wide vein-type mineralisation with pyrrhotite and minor chalcopyrite, pyrite, galena and sphalerite (Auer, 2022);
7. Burgfrieden: mineralisation with pyrrhotite, chalcopyrite, pyrite, arsenopyrite;
8. Leisach, „Eiserner Hut“: old trenches targeting arsenopyrite, pyrite and pyrrhotite in a gossean-type zone.

Greenfield prospection for tungsten in East Tyrol led to the discovery of several scheelite showings in the Thurntaler Complex (Höll, 1971; Krol, 1974). The largest one is located at Tafinalpe where a nowadays inaccessible exploration tunnel was driven up in 1978–79 (Neinavaie et al., 1983). Voest-Alpine AG carried out exploration between 1978 und 1987 in East Tyrol and a larger tungsten anomaly was found in the area to the south and southwest of Lienz (Hausberger et al., 1982; Thalmann et al., 1989). Higher contents of tungsten were analysed in stream sediments (heavy mineral concentrates, sedimentary fine fraction) as well as in soil and bulk rock samples. For the compilation of the data from several unpublished reports by Voest-Alpine AG see the appendices in the Master's thesis by Hutter (2022).

Investigating stream sediment anomalies with UV lamping led to the discovery of scheelite in outcrops, loose boulders and scree material (Voest-Alpine AG, 1979). The main W-mineralised areas are located between Edenwiese and Taxer Gassl and between Reiteralm and the upper station of the chairlift to Sternalm. Scheelite was observed as joint filling, disseminated and occasionally in quartz veinlets in the tonalite. It is also present in the massive sulphide ores at the Lienzer Schlossberg – Moosalm pyrrhotite mine. A bulk sample from these mine dumps yielded 831 ppm W and 610 ppm Cu. There, fine-grained disseminated scheelite is part of the sulphide assemblage hosted in contact metamorphic mica schist, micaceous quartzite and minor marble (Neinavaie, 1979; Fuchs, 1982; Neinavaie et al., 1983; Raith, 1983).

3. Methods

For optical microscopy, polished thin sections and blocks were investigated with polarisation microscopes by transmitted and reflected light (Olympus BX40, Zeiss axioLab with a Zeiss Evo digital camera). Back scattered electron (BSE) and cathodoluminescence (CL) imaging and the quantitative wave-length dispersive analyses

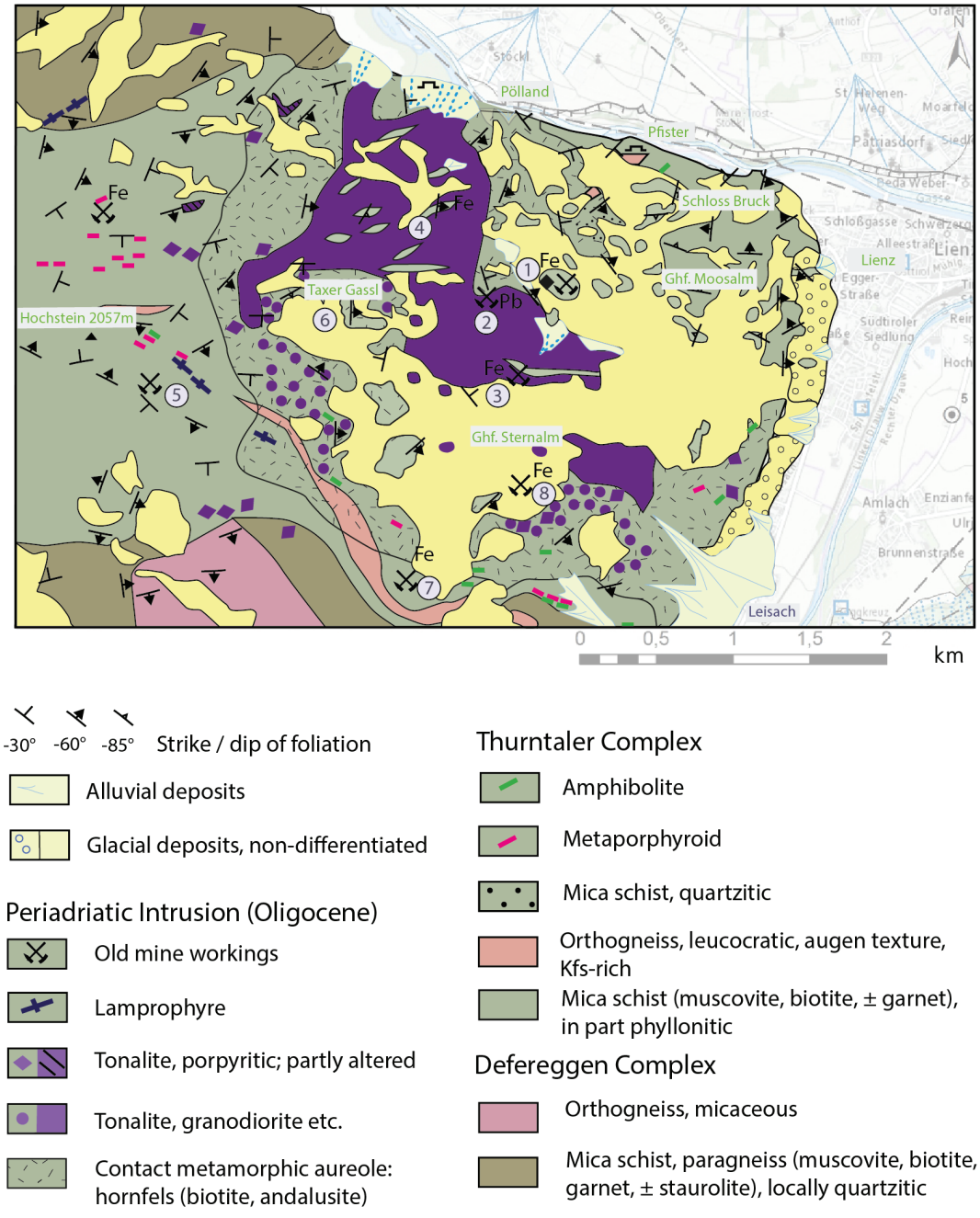

Figure 2: Geological map of the Lienz/Edenwald intrusion west of Lienz (after the geological map 1:50 000 by Linner, 2013). Old mine workings (IRIS database, Weber and Lipiarski, 2020): 1 = Lienzer Schlossberg – Moosalm; 2 = Hoferschacht; 3 = Tiefenriese; 4 = Wolfesbach; 5 = Hochstein; 6 = Taxer Gassl; 7 = Burgfrieden; 8 = Leisach Eiserner Hut.

(WDS) were performed with a Jeol JXA 8200 electron micro analyser installed at the Chair of Resource Mineralogy, Montanuniversität Leoben, Austria. For analytical conditions and detection limits the reader is referred to Hutter (2022).

Scanning Electron Microscope (SEM) based Mineral liberation analysis (MLA) was conducted at the Helmholtz Institute Freiberg for Resource Technology, Germany. A ThermoFisher Quanta 650F MLA system was used for EDX spectral mapping. It is equipped with two Bruker Quantax X-Flash 5030 energy-dispersive X-ray spectroscopy (EDX) detectors. Further information regarding the measurement procedure can be found in Altenberger et al. (2024).

Trace elements in scheelite were determined in the LA-ICP-MS laboratory of the Institute of Mineralogy at University of Münster, Germany. Analyses were performed on a Thermo Fisher Element XR HR-ICP-MS coupled to a Teledyne Photon Machines Analyte G2 193-nm ArF-based excimer laser ablation system. The analyses were measured with a spot diameter of 40 µm at 10 Hz with an energy of ca. 4 J/cm^2 for 40 s. The gas blank was previously determined for 20 s and sample washout was set to 15 s. The NIST SRM 612 reference glass (Jochum et al., 2011) was used as (primary) external reference material. Secondary reference materials included glass standards GSD-1G, GSE-1E (Jochum et al., 2005) and three matrix-matched in-house reference materials from the Felbertal deposit (Scheelite-A, Scheelite-B and Scheelite-S). All measurements on reference materials and unknowns were normalised to ^{43}Ca as the internal standard isotope before calibration for scheelite analysis. Calcium contents in scheelite were determined prior to LA-ICP-MS analyses using routine EPMA-WDS techniques at the same spots. Offline data processing and evaluation of trace elements were performed using the G.O.Joe software (Altenberger et al., 2023) to correct the abundance sensitivity of ^{182}W and ^{183}W on ^{181}Ta. For further details the reader is referred to the paper by Haupt et al. (2024). The results were filtered to remove analyses with internal 2 standard error (SE) greater than 30 % of the corresponding median of the signal and the threshold filter was set to 25 %. The analytical precision for most measured elements is better than 8 % and the results of the secondary reference material (GSD-1G and GSE-1E) agree with their literature values within ±10 %.

As confirmed by Sciuba et al. (2020) and Haupt et al. (2024), the accuracy is appropriate if NIST SRM 612 is used as primary reference material and ^{43}Ca as internal standard despite the different matrix composition of the scheelite. The preferred values for the reference materials are from the GeoReM database (Jochum et al., 2005). Limits of detection at 95 % confidence were calculated for all elements in each point analysis based on Poisson distribution statistics as recommended by Pettke et al. (2012).

Structural data were plotted with the Tectonic Data Analyser freeware of University of Graz (Stegmüller, 2022).

4. Scheelite mineralisation

Scheelite occurs in two different associations: (1) in retrograde skarn assemblages (i.e., disseminated scheelite in a massive pyrrhotite-dominated sulphide skarn and in sericite-calcite-chlorite fault rocks) and (2) along joints and in quartz stockwork veins in tonalite.

The old workings of an abandoned pyrrhotite mine are located about 1400 m SW of Schloss Bruck at an altitude of about 1100 m between Edenwald and Moosalm. The massive ore is exposed along 250 m in the abandoned

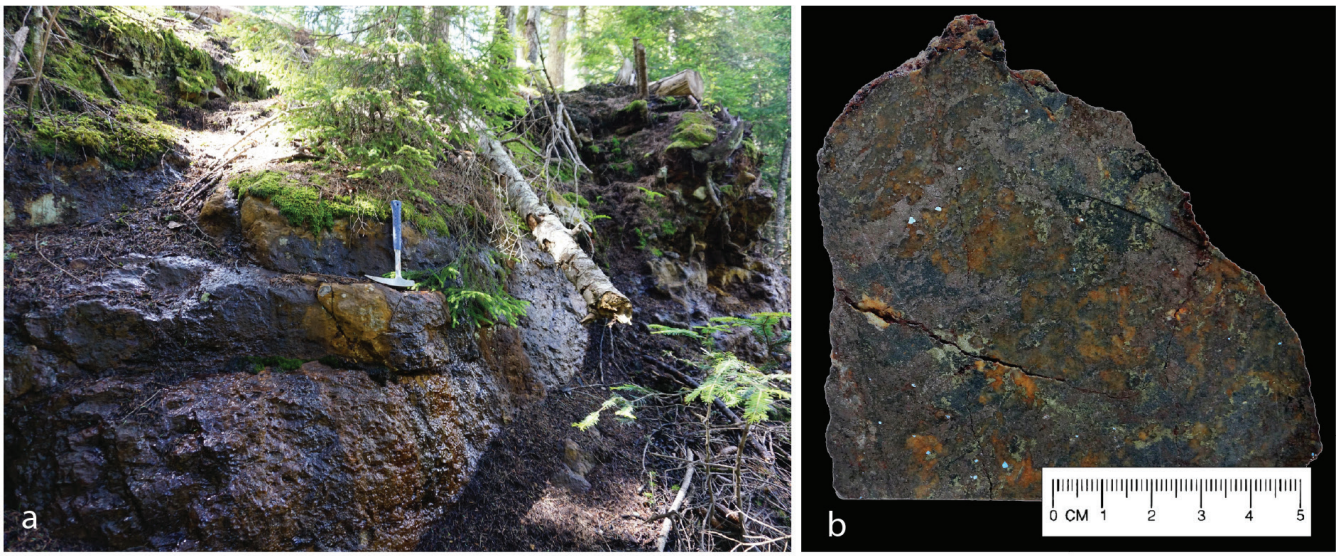

Figure 3: Massive sulphide skarn ore, pyrrhotite mine Lienzer Schlossberg – Moosalm. **(a):** Outcrop of ca. 1.5 m thick weathered massive sulphides in the abandoned open pit. **(b):** Slab of massive sulphide ore rich in pyrrhotite with disseminated fine-grained scheelite (light blue fluorescence), combined normal and short-waved UV light.

open pit and in two 25 m long underground workings (Fig. 3a). The estimated reserves of pyrrhotite are ca. 30,000 t (Fuchs, 1982). There is plenty of ore left on the dumps from the last mining activities dating back to 1919–1923. The ores are hosted in calc-silicate fels (clinopyroxene, plagioclase, quartz) forming concordant lenses in the pelitic hornfels and hornfels-gneiss (Linner, 2003). In the following we refer to this ore type as scheelite-bearing massive sulphide skarn.

The ore minerals of the massive sulphide skarn are pyrrhotite, chalcopyrite, sphalerite, galena, pentlandite, pyrite, native bismuth and scheelite (Figs. 3b, 4a-d). The main ore mineral is pyrrhotite. It is partly transformed to pyrite/marcasite (Fig. 4c, "Zwischenprodukt", Ramdohr, 1975). Lamellas in chalcopyrite were interpreted as inversion twins of high-temperature chalcopyrite ((Fig. 4b, Neinavaie, 1979; Fuchs, 1982). Larger pyrite crystals evidence cataclastic deformation and show reaction rims of goethite. Other minor minerals are sphalerite, galena and pentlandite; the latter occurs as flame-like exsolutions in pyrrhotite supporting its high-temperature origin (Kelly and Vaughan, 1983).

Scheelite forms tiny up to mm-sized crystals in the sulphide matrix and contains inclusions of pyrrhotite and chalcopyrite (Figs. 3b, 4a). Accessory phases are native bismuth, the rare bismuth-telluride hedleyite and electrum; other accessories are apatite and zircon (Fig. 4d; Auer, 2022). The gangue minerals of the ore are clinopyroxene, actinolitic amphibole, epidote, chlorite, Ca-rich plagioclase, and quartz. Minor and accessory minerals are titanite, ilmenite, apatite, allanite-(Ce) and monazite-(Ce).

Structurally controlled scheelite mineralisation is exposed in Unterbaustollen, one of the two still accessible underground galleries. It is found in an up to 0.5 m wide fault zone at the contact of the massive sulphide skarn to the silicified biotite-plagioclase hornfels. Euhedral scheelite crystals up to 1 cm in size and showing pyramidal morphology are embedded in a fine-grained matrix of sericite, calcite and chlorite (SCC vein) (Fig. 5a–d). Accessories are apatite, allanite-(Ce), titanite, and rutile (Fig. 5). Allanite forms larger euhedral crystals. Based on the mineralogy (sericite + chlorite + calcite), this mineral assemblage is interpreted to represent a low-temperature (T <300 °C) skarn vein.

The second type of scheelite mineralisation is found in the tonalitic intrusive rocks where scheelite forms millimetre thin coatings on joint planes ("Tapetenvererzung" = wallpaper-like; Fig. 6a). It is also present in disseminated form and in larger crystals in cm-thick quartz veinlets (Fig. 6b). The scheelite-quartz veins trend WNW-ESE with steep dip to SSE (Fig. 6c). The quartz veinlets are surrounded by cm-thick alteration selvages dominated by alkalifeldspar. Plagioclase is lacking in this alteration zone and biotite contents are lower than in the non-altered tonalite (Fig. 7a). These veins are interpreted as high-temperature veins with a cm-thick potassic alteration halo.

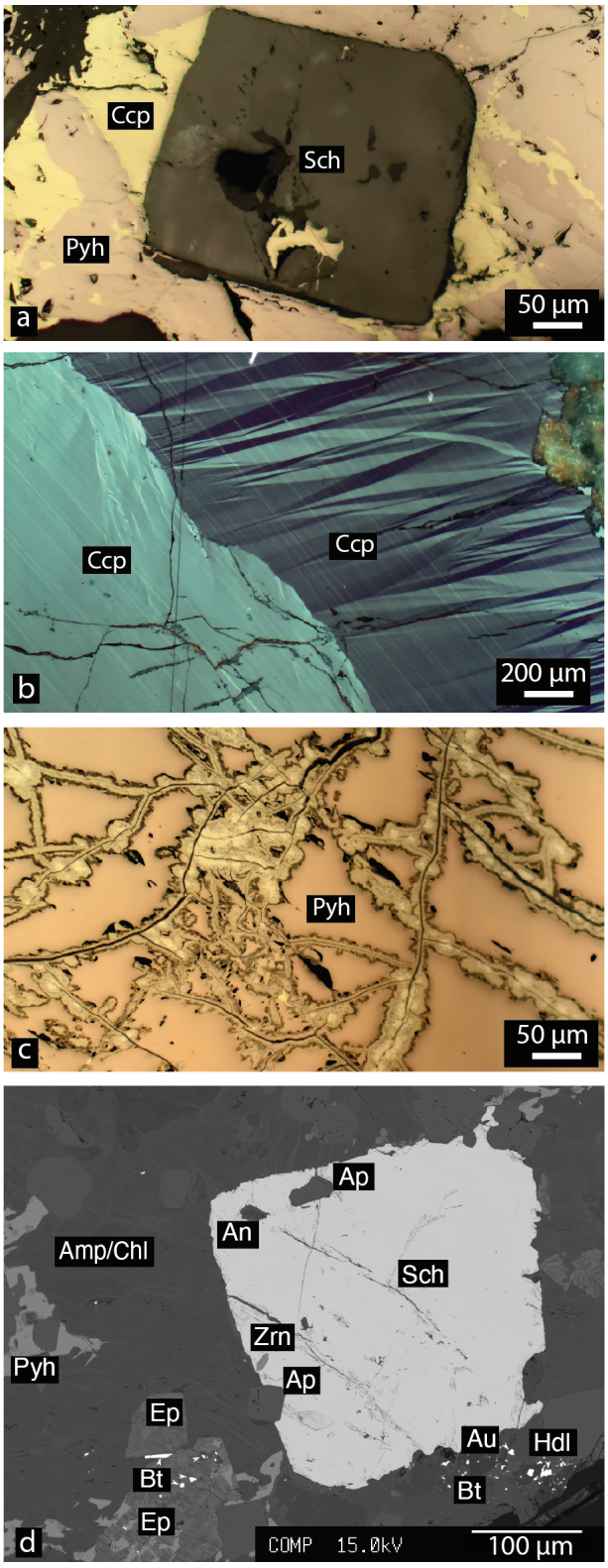

Figure 4: (a): Euhedral scheelite (Sch) with pyrrhotite (Pyh) and chalcopyrite (Ccp), reflected light and parallel polars, sample SB4a. **(b):** Lamellar twinning in chalcopyrite, reflected light and crossed polars, sample 87317. **(c):** Transformation of pyrrhotite into "Zwischenprodukt", a mixture of pyrite and marcasite, reflected light and parallel polars, sample SB16A. **(d):** BSE image showing scheelite associated with other accessories; Ap apatite, Zrn zircon, Bi native bismuth, Au electrum, Hdl hedleyite; the silicate matrix consists of anorthite (An), epidote (Ep), amphibole (Amp) and chlorite (Chl), sample 87317. Mineral symbols according to IMA-CNMNC (Warr, 2021).

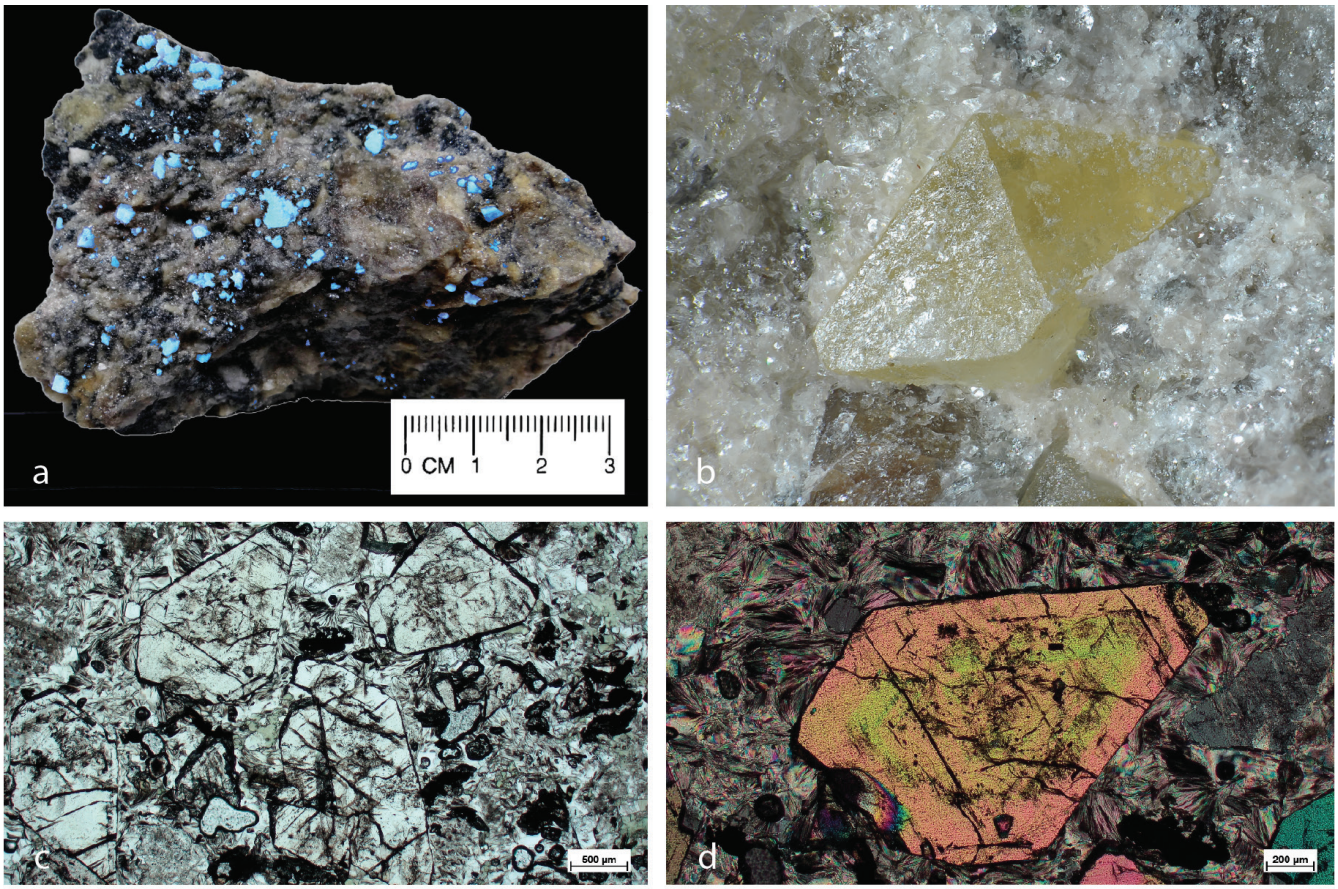

Figure 5: Scheelite rich calcite-chlorite-sericite rock, Unterbaustollen Lienzer Schlossberg – Moosalm. **(a):** Hand specimen in combined normal and short-waved UV light; scheelite shows bluish fluorescence colour, sample FH20 SB17A. **(b):** Euhedral scheelite crystal (ca. 5 mm) in matrix of calcite and phyllosilicates; photo C. Auer. **(c):** Euhedral scheelite (high relief) in thin section. The semi-opaque mineral is rutile; transmitted light and plane polarisers, sample FH20 SB17A. **(d):** Euhedral scheelite showing optical zoning. The matrix is sericite, chlorite and calcite; transmitted light and crossed polarisers, sample FH20 SB17A.

5. Skarn and related rocks

Less common lithologies that are intercalated in pelitic hornfels at Schlossberg are pyroxene-fels, calc-silicate fels, marble and hydrothermally altered tonalite. The dark and massive *pyroxene hornfels* (SB14B) is mainly composed of hedenbergite with less plagioclase; the latter can be concentrated in bands. Minor minerals are quartz and calcite, accessories are apatite, allanite-(Ce), zircon, scheelite, ilmenite, rutile, pyrrhotite, chalcopyrite. Native bismuth and non-identified silver-minerals were detected by EPMA. Scheelite forms up to 100 µm large individual crystals in the pyroxene-dominated assemblage.

An up to 1 m thick *marble* layer is exposed in the hanging wall of the massive sulphides in the abandoned open pit at Mooswiese. It is a coarse-grained banded calcite marble showing granoblastic texture. In the darker bands, calcite is associated with plagioclase, clinoamphibole (tremolite-actinolite), chloritised biotite, and epidote. The accessory opaque phases are Fe-sulphides, ilmenite, rutile and graphite.

Calc-silicate fels (SB14I) is developed between the tonalite and marble. It consists of domains rich in calcite alternating with domains containing grossular, diopsidic-hedenbergitic clinopyroxene, vesuvianite and wollastonite. Garnet and vesuvianite form larger crystals in the finer grained matrix of clinopyroxene and wollastonite. Calcite is present as inclusion in the large anhedral garnet but also in late calcite-quartz veinlets crosscutting the calc-silicate assemblage. Accessories are apatite, titanite, zircon, (up to 100 µm large) scheelite, pyrrhotite, chalcopyrite pentlandite and other Ni-As-(S-P) phases that were too small to be identified.

A dyke of hydrothermally altered tonalite (SB14F) is exposed in the open pit. The igneous assemblage consists of plagioclase, quartz, biotite, ilmenite (?) and in darker patches with relict clinopyroxene. The alteration transforms calcian plagioclase to more sodic compositions and leads to formation of secondary biotite. Newly formed calcian amphiboles are present in nests forming fibrous aggregates in the altered tonalite. Sericite, carbonates and chlorite are interpreted as the final low-temperature products of alteration. Accessories include ilmenite, titanite, rutile, allanite-(Ce), zircon and corundum. The opaque phases are pyrrhotite, minor chalcopyrite and rare sphalerite and silver.

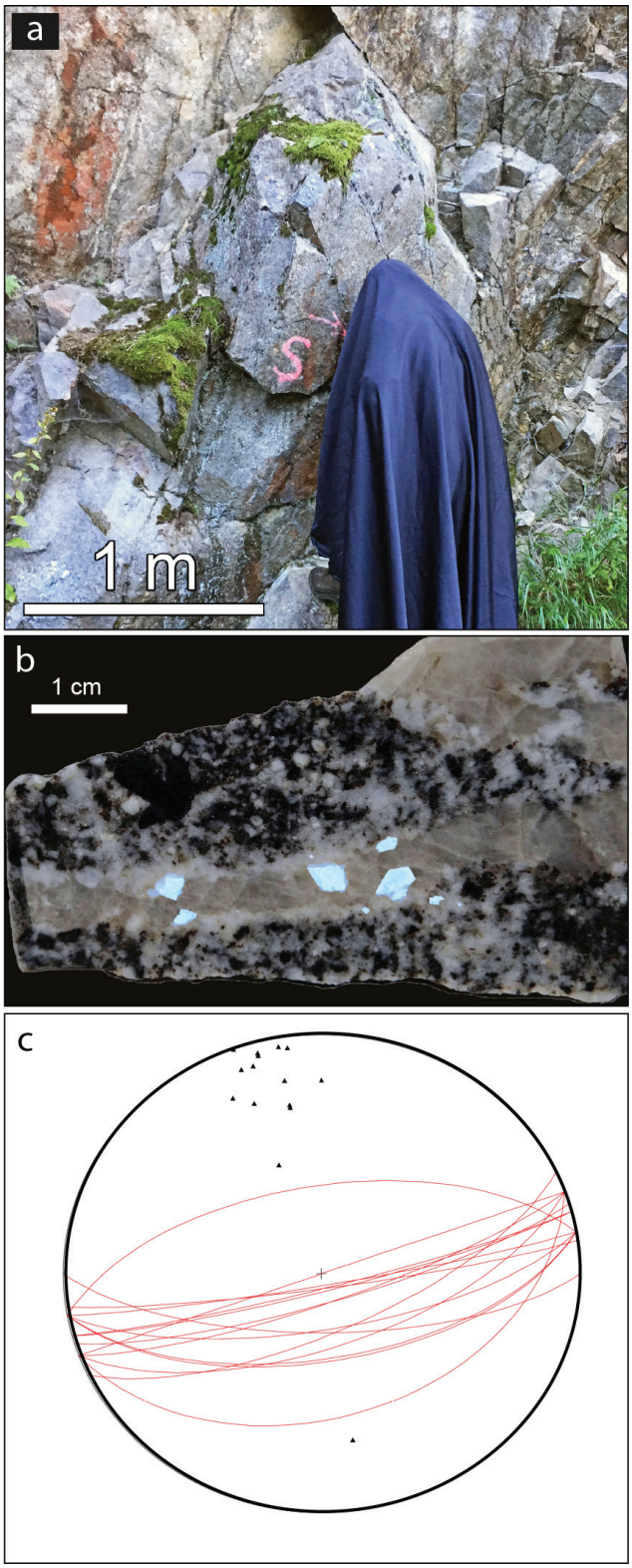

Figure 6: (a): F. Altenberger (working "undercover" with a light-tight blanket) inspecting an outcrop of jointed tonalite for scheelite using a UV-lamp. On some of these ENE-WSW-striking joint planes thin scheelite coatings ("Tapetenvererzung") were found during exploration by Voest-Alpine AG (marked S). **(b):** Scheelite-quartz veinlet in tonalite (plagioclase, biotite, quartz). Combined normal and short-wave UV light; scheelite shows blue fluorescence. Sample FA20 SB36. **(c):** Stereonet plot (poles and great circles) of quartz- and scheelite-quartz veins/veinlets hosted in tonalite. The plot was created with the Tectonic Data Analyser freeware (Stegmüller, 2022).

6. Mineral chemistry

6.1. Garnet

Garnet was analysed from the calc-silicate fels SB14I (Fig. 8a). Selected garnet analyses are listed in Table 1. Recalculation of ferric iron and calculation of garnet endmembers were made with the Excel spreadsheet by Locock (2008). Garnet is classified as grossular with variable andradite component; the latter varies between about 10 to 24 % (Fig. 8a). The contents of Mg, Mn and Fe^{2+} are low (0.x to few x mass %) and the combined endmembers of divalent cations (pyrope, almandine, spessartine) are less than 10 %. The small Ti content of garnet results in small numbers of Ti-garnet endmembers (morimotoite, hutcheonite; Tab. 1). The grossular-rich composition corresponds to those found in reduced tungsten skarns (Fig. 8a).

6.2. Clinopyroxene

Selected analyses of clinopyroxene from four different lithologies (SB14B/I/F, SB16a) are listed in Table 2 and compositions are shown in the diopside-hedenbergite-johannsenite triangle (Fig. 8b). All are calcic pyroxenes and members of the diopside-hedenbergite solid solution series with considerable variations in X_{Mg} and low contents of manganese and negligible sodium. In the calc-silicate fels (SB14I) where clinopyroxene coexists with grossular, vesuvianite and wollastonite it is classified as diopside (X_{Fe} 0.24-0.52; mean 0.40; n=10), in the retrograde sulphide skarn ore (SB16a) it has intermediate composition (X_{Fe} 0.38-0.77; mean 0.57; n=30) straddling between the diopside and hedenbergite fields. The iron richest compositions are found in the pyroxene-plagioclase hornfels (SB14B: X_{Fe} 0.87-0.98, mean 0.92, n= 63); these are exclusively hedenbergite. In the few clinopyroxene analyses from the altered tonalite X_{Fe} ranges from 0.32 to 0.40 (Fig. 8b).

6.3. Plagioclase

Plagioclase is a gangue mineral in the massive sulphide skarn (SB4a, SB16a) and a major mineral in the altered tonalite next to the W-bearing sulphide ores. Selected analyses are listed in Table 5 and the total analyses are illustrated in Figure 8c. Plagioclase in the massive sulphides is calcic (bytownite, anorthite) with small compositional variation; the X_{An} is 0.84 to 0.94 (mean 0.9 ± 0.2). Plagioclase analyses from the massive sulphide show Fe contents up to 1 mass %. Plagioclase from the altered tonalite shows a wider compositional variation with X_{An} from 0.32 to 0.94. A bi-polar distribution is seen in the data set with two maxima at about X_{An}80–90 and X_{An}40–50. The presence of two generations of plagioclase was confirmed by EPMA imaging. Plagioclase of intermediate composition overgrows or replaces the Ca-rich cores in the altered tonalite.

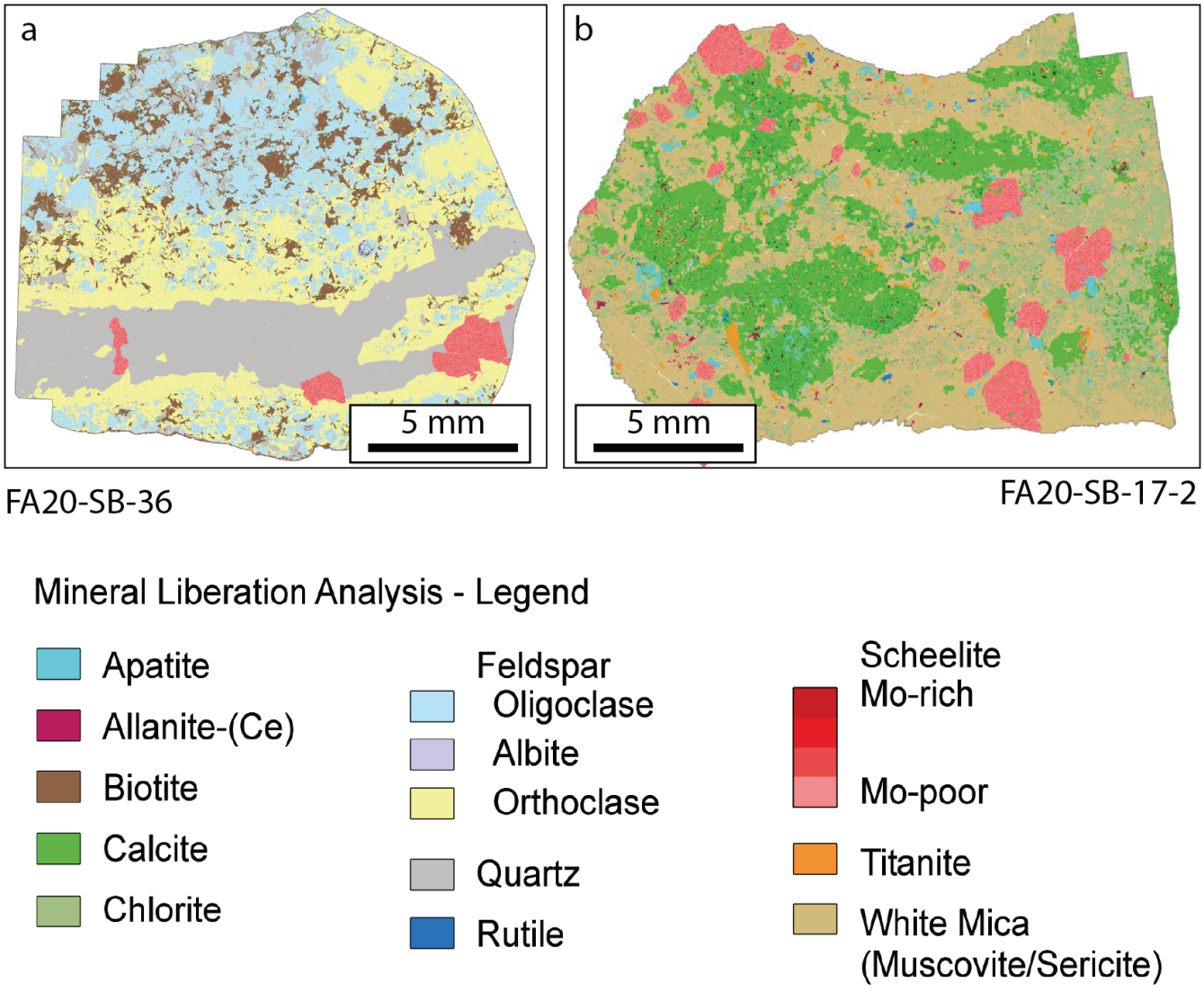

Figure 7: EDX spectral maps by SEM-based Automated Mineralogy (MLA). **(a):** Image of the specimen shown in Figure 6 (b). A potassic alteration zone with alkalifeldspar is developed in the vein selvage. Sample FA20 SB36. **(b):** Image showing the sericite-chlorite-calcite (SCC) association with scheelite, sample FA20 SB17-2 (see Fig. 5).

6.4. Vesuvianite

Vesuvianite is a complex calc-silicate mineral with the general formula $X_{19}Y_{13}Z_{18}T_{0-5}O_{68}W_{10}$ where X = Ca, Na, K, REE, Pb, Sb^{3+}, Bi, Th; Y = Al, Mg, Fe^{3+}, Fe^{2+}, Ti, Mn, Cu, Zn; Z = Si; T = B; W = OH, F, Cl, O. The X site is occupied by Ca, close to 19 atoms per formula unit (a.p.f.u.; Groat et al., 1992). Occupancy of the Y site depends on whether vesuvianite contains B or is B-free. In the B-free vesuvianite, between 8 and 11 a.p.f.u. of Al are incorporated, whereas in B-bearing one, it is only 6 to 7 a.p.f.u. Al. The W position is mainly occupied by OH groups, but F, Cl and O can also substitute for OH. A consequence of the possible O substitution in the W site is that the number of negative charges is not constant. Charge balance for the additional O is obtained by substitution of trivalent cations in the Y site (Groat et al., 1992). As neither the water content nor the Fe^{3+}/Fe^{2+} is known from EPMA analyses the number of O in the W position and the valence of iron cannot be recalculated. For the calculations it is assumed that all 10 W sites are filled with (OH, F, Cl) and water is calculated via target value search. Iron is treated as Fe^{2+}.

About 30 analyses of vesuvianite were made in sample SB14I, the calc-silicate fels in which vesuvianite coexists with grossular, clinopyroxene, wollastonite and calcite (Tab. 3). Cation variations are best illustrated in a plot of the cations in the Y site plotted versus Al; a clear negative correlation is to be seen (Fig. 9a). The Si values vary from 17.8 to 18.3 a.p.f.u., on average 18.0; i.e., close to the ideal value. Of the other cations, only titanium shows some larger variation. It is noteworthy that vesuvianite from Schlossberg contains from 0.4 to 1.8 mass % fluorine. Hence, in the formula 0.7 to 2.8 a.p.f.u. of the anions is F (mean 1.7). Chlorine is 0.1 a.p.f.u. The remaining W sites are assumed to be OH. Neglecting O in the W site (see above), the average formula of vesuvianite from Schloss-

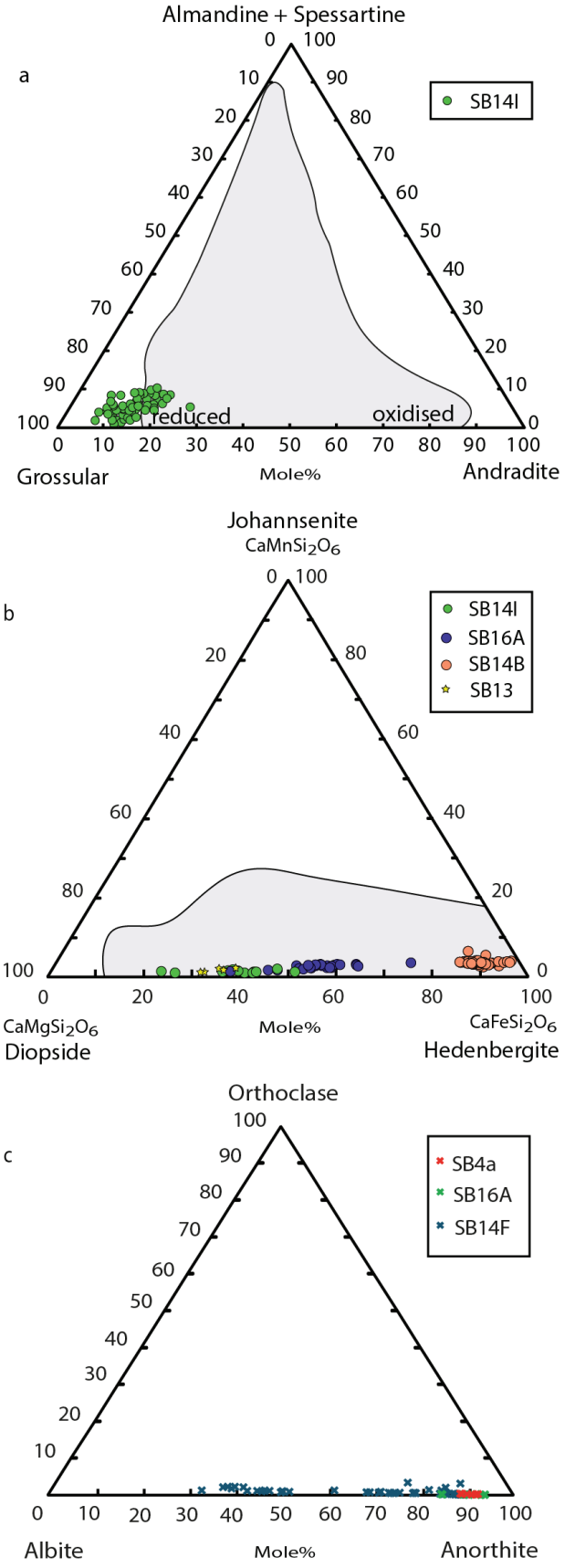

Figure 8: Triangular diagrams showing composition of **(a):** garnet from anhydrous garnet-clinopyroxene-vesuvianite-wollastonite skarn, Sample SB14I. **(b):** clinopyroxene from different parageneses (see text for details). **(c):** feldspars; Fields of tungsten skarns in (a) and (b) are from Meinert (1992).

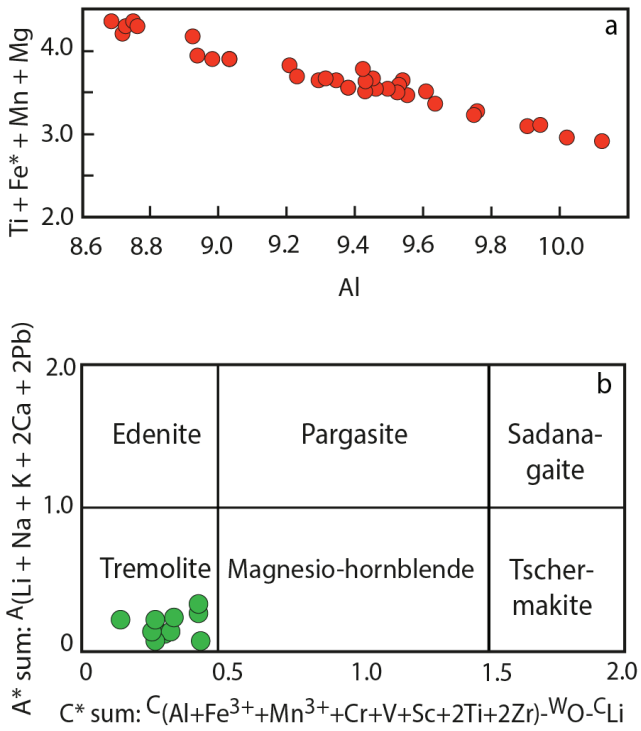

Figure 9: (a): Al vs. (Ti+Fe*+Mn+Mg) plot showing compositional variation of vesuvianite. **(b):** Classification diagram C* sum [^{C}(Al+Fe^{3+}+Mn^{3+}+Cr+V+Sc+2Ti+2Zr)-^{W}O-^{C}Li] vs. A* sum [^{A}(Li + Na + K + 2Ca + 2Pb)] of amphiboles from the massive sulphide skarn.

berg can therefore be given as $Ca_{18.7}(Mg_{1.3}Fe_{1.7}Ti_{0.6}Al_{9.4})Si_{18}O_{68}[(OH)_{8.2}F_{1.7}Cl_{0.1}]$.

6.5. Amphiboles

Amphiboles are a common gangue mineral in the massive sulphide skarn. Selected analyses of two samples (SB4a, SB16a) are listed in Table 4. The formula and nomenclature were calculated using an Excel spreadsheet (Locock, 2014) following the IMA 2012 amphibole classification (Hawthorne et al., 2012).

The general formula of the amphibole supergroup can be written as $AB_2C_5T_8O_{22}W_2$ with

A = □, Na, K, Ca, (Pb, Li);
B = Na, Ca, Mn^{2+}, Fe^{2+}, Mg, (Li);
C = Mg, Fe^{2+}, Mn^{2+}, Al, Fe^{3+}, Mn^{3+}, Ti^{4+}, (Cr^{3+}, Li);
T = Si, Al, Ti^{4+}, (Be);
W = OH, F, Cl, (O^{2-}).

The amphiboles are all members of the calcic (OH, F, Cl) subgroup. Only up to 16 % of the A site are occupied. Iron and magnesium are the dominant cations in the C site with minor aluminium. Thus, the amphiboles are classified as ferro-actinolite (SB16a; Tab. 4) and actinolite (SB4a), respectively, and in the A* vs. C* diagram they plot in the tremolite field (Fig. 9b).

mass %	SB14I An3	SB14I An17	SB14I An21	SB14I An29	SB14I An42	SB14I An54	SB14I An71	SB14I An96	SB14I An97
SiO_2	39.14	38.93	38.85	39.03	38.28	38.21	38.19	38.14	37.85
TiO_2	0.33	0.52	0.28	0.68	0.58	0.14	0.39	0.25	0.32
Al_2O_3	19.36	18.46	20.03	20.15	17.79	17.62	18.08	18.09	17.55
FeO (T)	4.81	6.10	3.70	3.40	7.48	7.68	7.71	7.44	7.93
MnO	0.15	0.28	0.11	0.21	0.37	0.42	0.45	0.47	0.40
MgO	0.26	0.16	0.31	0.40	0.15	0.12	0.14	0.09	0.15
CaO	35.70	34.64	36.00	35.97	34.34	34.37	34.42	33.80	34.48
Na_2O	0.00	0.01	0.01	0.05	0.01	0.02	0.00	0.00	0.02
Total	99.74	99.09	99.29	99.88	99.00	98.58	99.37	98.28	98.69
Recalculated									
FeO	0.75	2.01	0.00	0.05	1.59	1.04	1.21	1.90	0.60
Fe_2O_3	4.51	4.54	4.11	3.73	6.54	7.38	7.22	6.16	8.15
Total	100.19	99.55	99.70	100.26	99.65	99.32	100.10	98.90	99.51
End-members, mole %									
Grossular	0.833	0.794	0.870	0.859	0.746	0.756	0.754	0.763	0.747
Andradite	0.129	0.132	0.103	0.096	0.187	0.194	0.183	0.171	0.201
Spessartine	0.003	0.006		0.004	0.008	0.009	0.010	0.010	0.009
Pyrope	0.010	0.005	0.012	0.015	0.006	0.005	0.005	0.003	0.006
Almandine	0.016	0.034		0.001	0.034	0.022	0.026	0.041	0.013
Hutcheonite	0.009		0.008	0.019	0.017	0.004	0.011	0.007	0.009
Morimotoite	0.001	0.028							

Table 1. Selected analyses of garnet from calc-silicate fels SB14I; endmember calculation according to Locock (2008).

6.6. Pyrrhotite

About 140 analyses of four samples from the Schlossberg open pit (SB4a, SB16a, SCH5 und 87317) and one sample (SCH3) from the abandoned quarry Pfister were analysed by EPMA. Selected analyses are listed in Table 6. For the complete data set see the Master's thesis by Hutter (2022). The Co content varies from 0.06 to 0.15 (mean 0.11) mass %. The Ni and Cu contents are below or close to the detection limit of 0.02 mass %. Hence, pyrrhotite is classified as Ni-poor. The composition of pyrrhotite is non-stoichiometric with Fe ranging from 0.86 to 0.98, calculated on the basis of 1 S atom (Fig. 10a, b). There is some variation among the samples. The lowest Fe/S values of 0.86-0.90 is found at quarry Pfister (SCH3) whereas the analyses from Schlossberg are higher. Sample 87317 from the southern part of the mine has 0.88 to 0.90, sample SB16a has 0.88 to 0.94 with a maximum at 0.92 ± 0.01. Sample SCH5 yields similar values. The highest Fe/S values are seen in sample SB4a ranging from 0.90 to 0.96 with four outliers up to 1.0 (Fig. 10a).

Several structural types of pyrrhotite are known characterised by different Fe:S ratios. Stoichiometric troilite with ideal composition FeS has a 2C structure (Evans, 1970; Becker et al., 2010). The letter C refers to the number of NiAs-type unit cells, which are the basic building unit of the superstructures of the pyrrhotite group. The magnetic monoclinic 4C structural type has the ideal composition Fe_7S_8 (Tokonami et al., 1972). The 5C type has the ideal composition Fe_9S_{10} (de Villiers et al., 2009), the 6C type $Fe_{11}S_{12}$ (Villiers and Liles, 2010); the latter two are non-magnetic. These superstructures are no true polytypes as the layers are variably occupied. Hence, the exact Fe:S ratios are not reached but there are compositional ranges. For 4C, the range of Fe:S is between 0.855 and 0.885 (ideally 0.875, Fe_7S_8), for 5C between 0.885 and 0.91 (ideally 0.90, Fe_9S_{10}) and for 6C between 0.91 and 0.94 (ideally 0.917, $Fe_{10}S_{11}$; Fig. 10a, b); Villiers and Liles, 2010). Ratios between 0.94 and 1 indicate mixtures of the 2C and 6C types, values around 1 troilite (Becker et al., 2010). Mixtures of 5C and 6C do also exist (Villiers and Liles, 2010).

Regarding our data set, pyrrhotite from quarry Pfister is of the magnetic type 4C. In sample 87317, 5C is dominant. In the other samples, type 5C and 6C are present. Microscopically, these structural types cannot be distinguished; distinction based on optical properties is problematic (Ramdohr, 1975). In addition, the overlapping Fe:S ratios suggest that mixtures of e.g., types 5C and 6C are present.

7. Scheelite micro-texture and trace elements

Trace element contents of scheelite of four samples from the different mineralisation types (Chapter 4) were analysed by LA-ICP-MS (Tab. 7) and the scheelite micro-texture was documented with CL images, including the analysis spots (Fig. 11a-d). The REE patterns of scheelite are illustrated in Figure 12.

For descriptive purposes and considering the REE patterns five micro-textural scheelite types were distinguished. They are referred to as Scheelite 1a, 1b, 2a, 2b, and 3 in the following. All scheelite types show blue fluorescence in short-wave UV light. Scheelite from the quartz-K-feldspar veinlets in tonalite shows superb os-

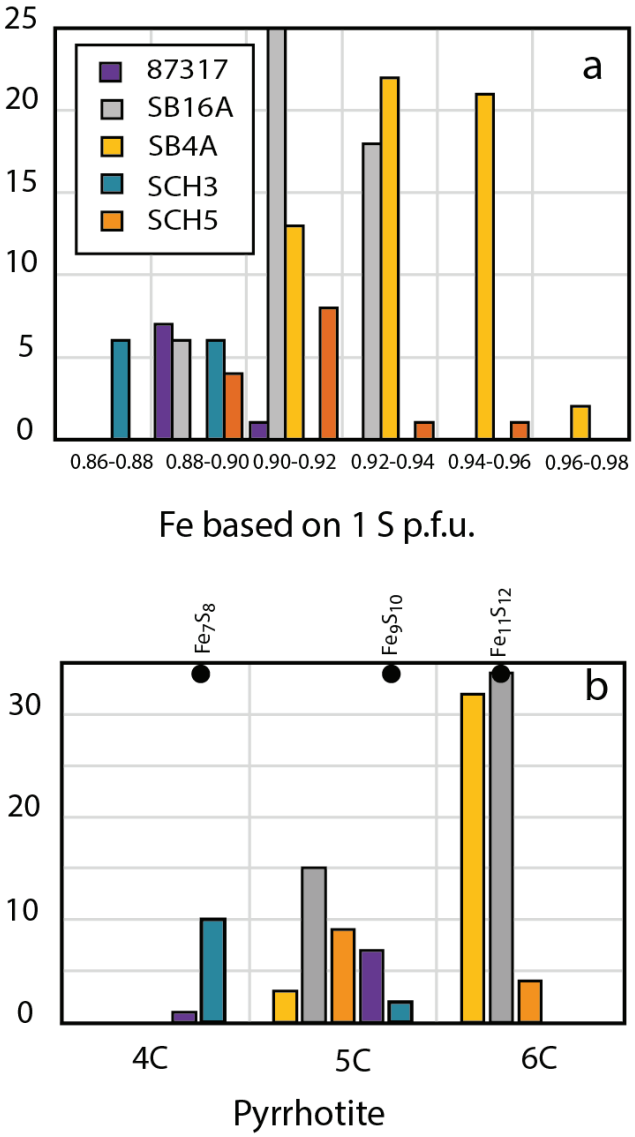

Figure 10: Composition of pyrrhotite. **(a):** Histogram of atoms of Fe based on 1 S; **(b):** Pyrrhotite polytypes (4C, 5C, 6C) and formulas of ideal compositions (black circles).

cillatory growth zoning and is named Scheelite 1a because it does not show any hints of hydrothermal overprint (Fig. 11 a). The "wallpaper"-type Scheelite 1b from the joints in the intrusive rock consists of CL-darker and CL-brighter zones and indicates very weak zonation in places (Fig. 11b). The disseminated scheelite from the massive sulphide ore exhibits CL-darker cores (Scheelite 2a) grading into oscillatory zoned scheelite (Scheelite 2b) that is overgrown or replaced by CL-brighter scheelite material (Scheelite 3, Fig. 11c). The latter forms by a dissolution-reprecipitation process. Eu- to subhedral scheelite crystals from the sericite-calcite-chlorite (SCC) skarn vein reveal oscillatory zoning (Scheelite 2a–2b) and dissolution reprecipitation features (Scheelite 3), similar to disseminated scheelite from the massive sulphide skarn ore (Fig. 11d).

The chondrite-normalised REE patterns of Scheelite 1a from the quartz-K-feldspar vein are enriched in light REE (LREE) over the intermediate REE (MREE) and depleted in heavy REE (HREE), resulting in dextral inclined profiles (Fig. 12a). Patterns of "wallpaper"-type Scheelite 1b from the joints show higher HREE contents than Scheelite 1a and have slightly convex (MREE-dominated) shapes (Fig. 12b). Scheelite 1a and 1b patterns are characterised by distinct negative Europium (Eu) anomalies (i.e., $Eu_A = Eu_{CN}/Eu^*_{CN}$, where $Eu^*_{CN} = [Sm_{CN} \times Gd_{CN}]^{0.5}$).

The REE patterns of disseminated scheelite from the massive sulphide skarn are typically convex with enrichment of the MREE and depletion of LREE and HREE (Fig. 12c). An evolution of the REE patterns can be established on the grain-scale. Scheelite 2a cores show the highest ΣREE, the strongest depletion in LREE and the most pronounced negative Eu anomaly (Eu_A = 0.13). In the oscillatory zoned Scheelite 2b, the ΣREE content, the LREE depletion and the negative Eu anomaly (Eu_A = 0.15 to 0.33) decrease. In the CL-bright reprecipitated Scheelite 3, the ΣREE contents may decrease by two orders of magnitude and the Eu anomaly is weakly negative to neutral (Fig. 12c). The patterns of scheelite from the SSC veins are comparable to those of Scheelite 2a, 2b, and 3 of the disseminated scheelite in the massive sulphide horizon (Fig. 12d). The pattern evolution resembles the previously described trend; again, a decrease of the negative Eu anomaly and a change towards slightly positive values with lower ΣREE is visible.

8. Discussion

8.1. Trace elements in scheelite

The correlation of CL-textures, trace element contents and Eu anomalies were examined by combined imaging and spot analyses in scheelite. CL revealed internal micro-textures which are dominated by oscillatory zoning what reflects fluctuating fluid conditions in hydrothermal systems (Shore and Fowler, 1996; Poulin et al., 2016). Prolonged hydrothermal activity is indicated by dissolution-replacement and overgrowth textures reworking the primary zonation (Putnis, 2002). Similar micro-textural observations have been described from scheelite in the Felbertal deposit (Haupt et al., 2024). These processes caused several types of scheelite (i.e., Scheelite 1–3) with distinct chemical compositions and REE patterns (Fig. 12a–d).

The distribution of REE in Scheelite 1a from quartz-K-feldspar veinlets illustrates a distinct HREE-depleted profile with negative Eu anomalies. "Wallpaper"-type Scheelite 1b presents slightly convex REE patterns with pronounced negative Eu anomalies resembling patterns of Scheelite 2b in the sulphide skarn assemblage. The patterns in scheelite from both joints and veinlets show little variation in ΣREE (Fig. 12a–b), possibly indicating a transient pulse of mineralisation without a pronounced fractionation of trace elements and the absence of other REE-incorporating phases.

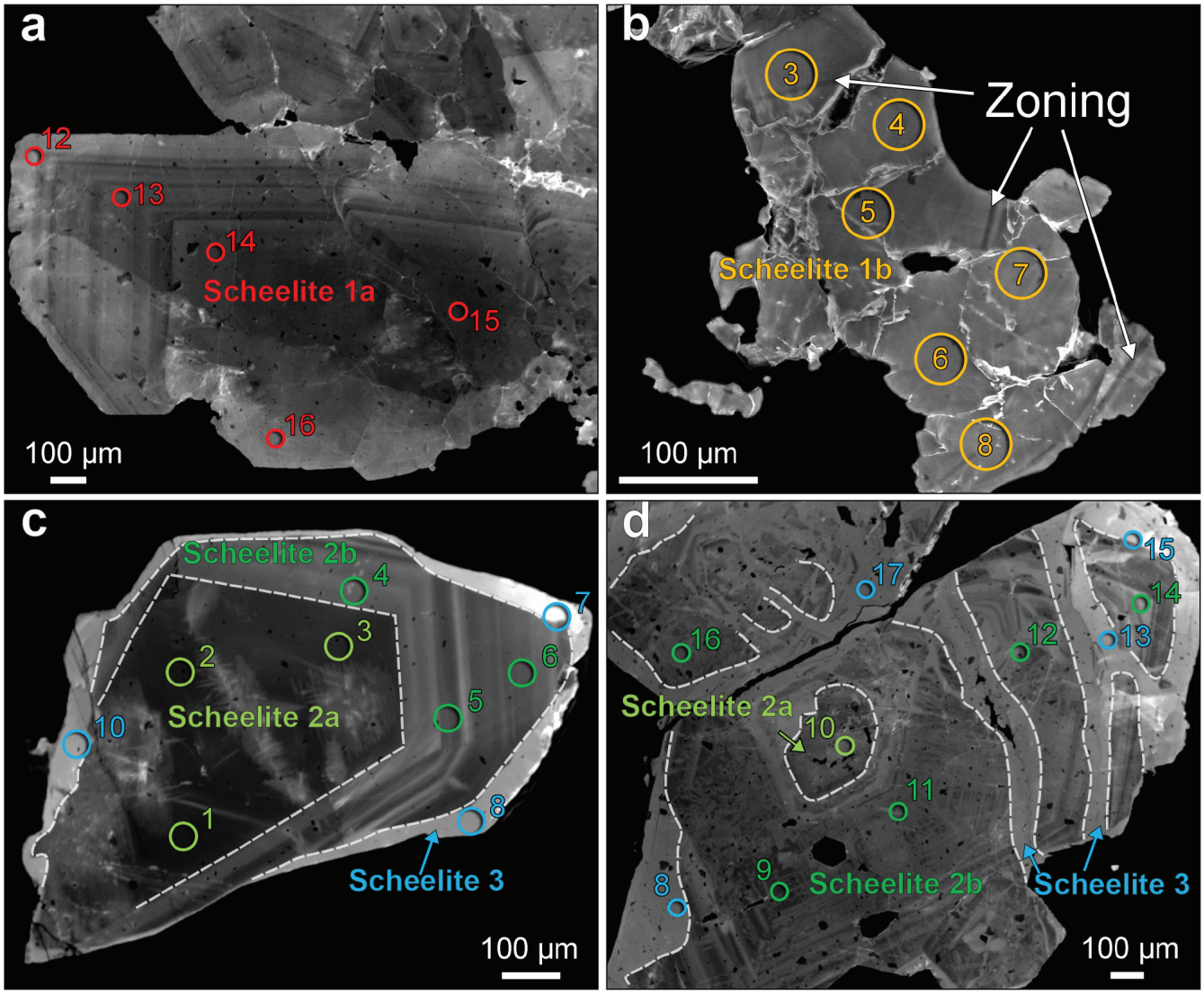

Figure 11: Cathodoluminescence (CL) images of scheelite from mineralized structures in tonalitic host rocks (a, b) and skarn assemblages (c, d). **(a):** Scheelite from quartz veinlets shows distinct zoning (Scheelite 1a). **(b):** Weak zoning patterns are visible in "wallpaper"-type scheelite formed on joints (Scheelite 1b). **(c):** Scheelite from the massive sulphide skarn shows a dark luminescent core (Scheelite 2a) grading into oscillatory zoned scheelite (Scheelite 2b) that is overgrown or replaced by CL-bright scheelite material (Scheelite 3). **(d):** Scheelite from sericite-calcite-chlorite fault rocks (SCC vein) exhibits similar micro-textures as described in (c); in addition, Scheelite 3 dissects Scheelite 2a–2b.

In contrast, the evolution of REE patterns in scheelite from the skarn assemblages comprises strongly convex (i.e., MREE-enriched) fractionation patterns with distinct negative Eu anomalies, which grade into slightly convex REE profiles that evolve into flat patterns with lower ΣREE and variable Eu anomaly at the outermost rims. The highest ΣREE contents occur in the CL-dark Scheelite 2a cores that continuously decrease across the oscillatory zoned Scheelite 2b towards the CL-bright rims of Scheelite 3 (Fig. 11c-d). Cross-cutting CL-bright domains also belong to Scheelite 3 and have the lowest ΣREE content (Figs. 11d, 12d). The evolution from Scheelite 2a and 2b to Scheelite 3 could reflect REE fractionation. One explanation could be gradual cooling of the hydrothermal system, in which the REE are continuously sequestered and the MREE are preferentially incorporated by scheelite (Poulin et al., 2018). Alternatively, the REE distribution might also be influenced by co-precipitating minerals in the skarn assemblage, which compete with scheelite particularly for the LREE (Raimbault et al., 1993; Poulin et al., 2018; Haupt et al., 2024). To explain the decrease in HREE observed in Scheelite 1 from the tonalite-hosted quartz vein, a HREE fractionating phase like xenotime or garnet should coexist with scheelite. Garnet has not been observed in the intrusive rocks at Lienz but it has been reported from other tonalite intrusions along the Periadriatic Fault System (Neubauer et al., 2018).

High Na (3.6–470 µg/g) and Nb (5.0–500 µg/g; Table 7) contents and the positive correlation of ΣREE+Y vs. Na+Nb+Ta (Fig. 13a) suggest that the main exchange vector for the incorporation of REE^{3+} in scheelite is via the combination of two coupled substitution mechanisms: (1) $2Ca^{2+}$

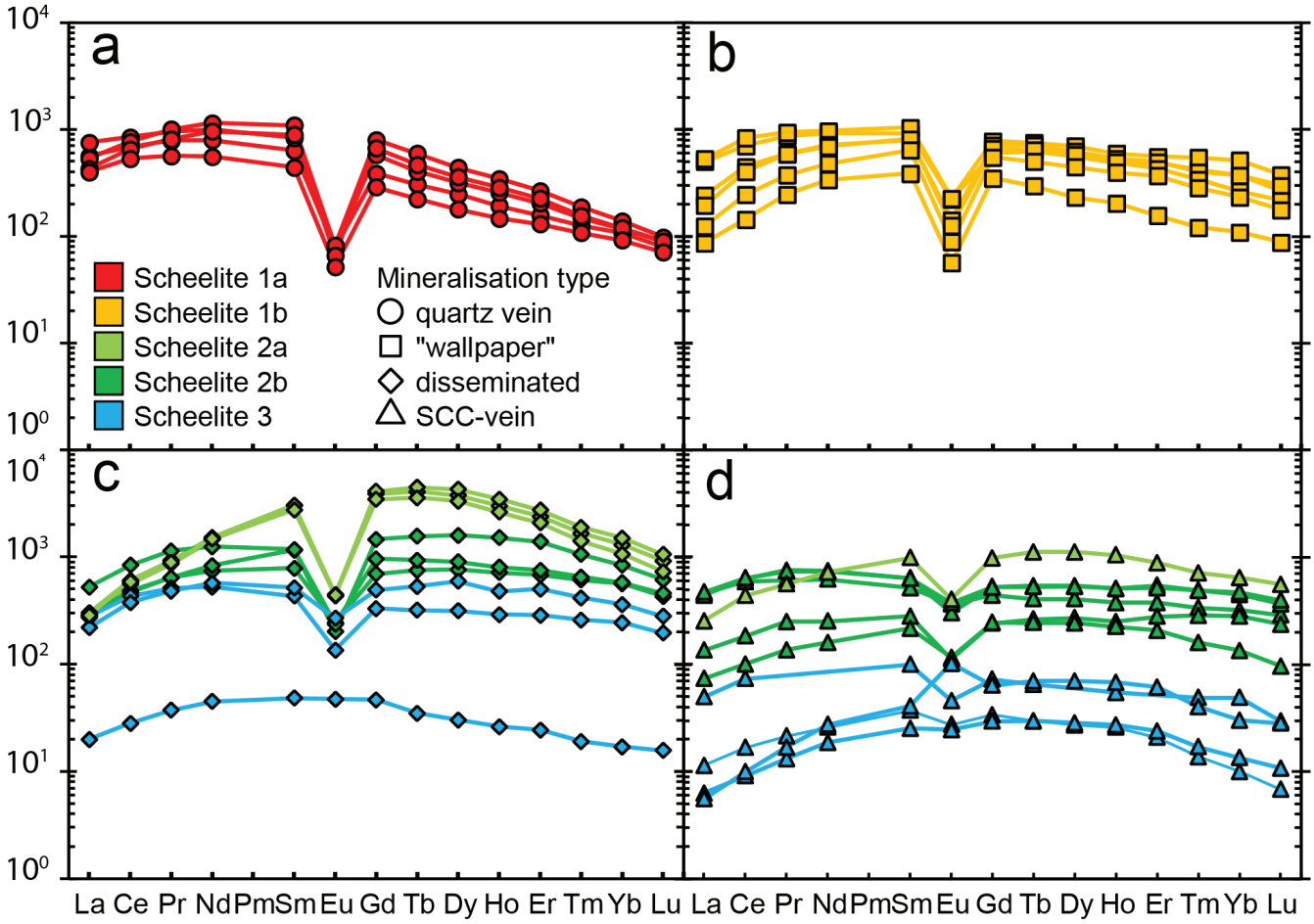

Figure 12: Chondrite-normalised REE plots of scheelite. **(a):** Scheelite 1a in tonalite-hosted quartz veinlets shows light REE-rich and heavy REE-depleted patterns with dextral inclined profiles. **(b):** Patterns of Scheelite 1b ("wallpaper") are slightly convex with negative Eu anomalies. **(c, d):** Scheelite patterns in skarn assemblages are typically convex with enrichment of the middle and depletion of light and heavy REE. A clear evolution of the patterns towards decreasing ΣREE contents from Scheelite 2a–2b to Scheelite 3 can be observed. See text for discussion.

$\leftrightarrow Na^{+} + REE^{3+}$ and (2) $Ca^{2+} + W^{6+} \leftrightarrow REE^{3+} + Nb^{5+}$. While the analyses of Scheelite 1a and 1b plot well on the 1:1 line, the higher ΣREE+Y contents in Scheelite 2a, 2b and 3 from the skarn assemblage suggests that a third substitution mechanism (3) $3Ca^{2+} \leftrightarrow 2REE^{3+} + \square_{Ca}$ (where $\square_{Ca}$ is a Ca site vacancy) likely also took place (e.g., Nassau and Loiacono, 1963; Ghaderi et al., 1999).

Regarding the evolution of the Eu anomaly, the Eu^{2+}/Eu^{3+} ratio, which has been used as a proxy of the redox potential, strongly depends on the temperature of hydrothermal fluids. At temperatures above 250 °C, Eu^{2+} should predominate in solution (Sverjensky, 1984; Bau, 1991). In case of the coupled substitution of the REE with Na or Nb as described above, the trivalent REE are favoured to substitute for Ca in scheelite. Hence, Eu should behave differently under reducing conditions with respect to the other REE^{3+} because Eu^{2+} has no charge-compensating effect to maintain electrostatic neutrality in the scheelite lattice and it has a larger ionic radius compared to Eu^{3+} (Ghaderi et al., 1999; Brugger et al., 2008). This results in a distinctive negative Eu anomaly as visible in scheelite from the quartz veinlets and joints (i.e., Scheelite 1a and 1b) as well as in Scheelite 2a and 2b from the sulphide skarn assemblage (Fig. 12). A decrease of the Eu anomaly amplitude in late Scheelite 3 is only observed in the skarn scheelite and reflects a decrease of Eu^{2+}/Eu^{3+} in the hydrothermal fluid (Fig. 12c–d). This may indicate a trend towards more oxidising conditions (increase of fO_2) in the gradually cooling hydrothermal system (Sverjensky, 1984).

Although scheelite at Lienzer Schlossberg has one of the highest ΣREE+Y contents in the Eastern Alps (F. Altenberger, unpublished data base), it contains less Mo (mean 120 µg/g; Tab. 7) compared to scheelite from the Felbertal deposit or the oxidised skarn-type W-(Sn) mineralisation at Messelingscharte, where Mo contents in scheelite can reach several mass % (Eichhorn et al., 1997; Ordosch et al., 2019; Haupt et al., 2024). The uptake of Mo in scheelite depends on the Mo concentration of the fluid but also on the redox conditions of the ore-forming fluids (Jensen et al., 2022; Miranda et al., 2022). Since mineral assemblages at Schlossberg point to a reduced skarn, it can be expected that Mo^{4+} replaces W^{6+} in scheelite only to a limited extent, what is consistent with other reduced tungsten skarn systems (Hsu, 1977; Jensen et al., 2022; Miranda et al., 2022).

The highest Mo contents (700–1,000 µg/g; Tab. 7) are

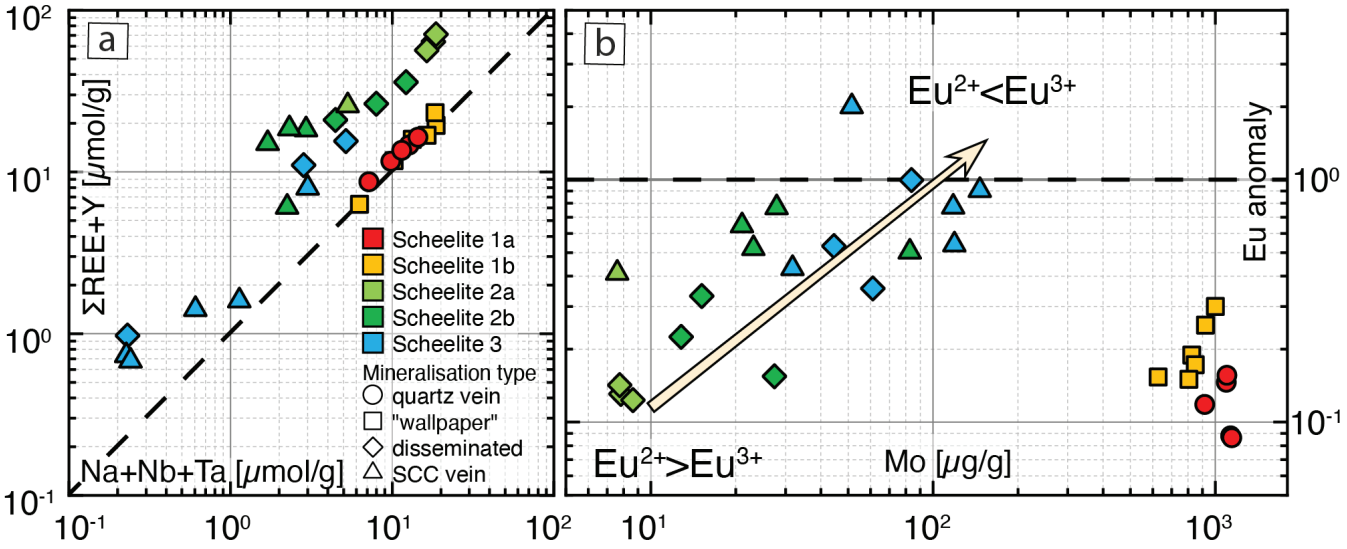

Figure 13: (a): Bivariate plot of ΣREE+Y vs. Na+Nb+Ta illustrating possible coupled substitution mechanisms in scheelite. **(b):** Plot of Mo vs. Eu anomaly (= Eu_{CN}/Eu^*_{CN}; $Eu^*_{CN} = [Sm_{CN} \times Gd_{CN}]^{0.5}$) indicating increase in redox conditions during scheelite crystallisation (arrow).

found in Scheelite 1a and 1b from quartz veinlets and joints ("wallpaper"), respectively, within the tonalitic host rocks. Their similar Mo contents suggest a genetic relationship of the two subtypes. The observation of potassic alkalifeldspar alteration selvages around quartz veinlets indicates formation during the early high-temperature stage of ore formation that is similar to the potassic alteration in porphyry Cu-Mo systems (e.g., Seedorff et al., 2005). Scheelite in the skarn assemblages has the lowest Mo contents and its complex CL-textures document a prolonged activity of the hydrothermal system (Tab. 7; Fig. 11c-d). Molybdenum shows an increase from 10 µg/g in Scheelite 2a to 100 µg/g in Scheelite 3 (favouring the stability of the oxidised Mo^{6+}) and a positive correlation with the Eu anomaly (Fig. 13b).

Based on the mineral chemistry of scheelite, we propose that tungsten mineralisation in the Lienz area comprises two phases. The first phase is linked with a high-temperature, REE- and Mo-richer fluid forming scheelite with higher Mo contents (up to 1000 µg/g, Tab. 7) in joints and quartz veinlets and associated with potassic alkalifeldspar alteration (i.e., Scheelite 1a and 1b). The second phase is linked with formation of the retrograde skarn assemblages with Mo-poor scheelite disseminated in the massive sulphide ore (i.e., Scheelite 2a, 2b, and 3). Scheelite in the fault rocks with sericite-chlorite-calcite (SCC vein) and the nearby massive sulphide skarn are comparable in respect of CL-textures and mineral chemistry (Figs. 11c-d, 12c-d, 13a-b). This second phase represents a subsequent lower temperature mineralisation pulse that is linked with sericite-carbonate (phyllic) alteration. Comparable Eu anomaly values for Scheelite 1 and Scheelite 2 indicate small differences in redox conditions between early tonalite-hosted mineralisation and the initial phase of late retrograde skarn mineralisation. The positive correlation of Mo contents and the Eu anomaly in Scheelite 2 and Scheelite 3 from the skarn assemblage suggests an evolution of the hydrothermal system towards more oxidising conditions during the final phase of ore formation (Fig. 13b).

8.2. The tungsten mineralising system

As presented in this paper, different styles of tungsten mineralisation have been documented in the area around Lienz in East Tyrol. These contain a sequence of scheelite types, which are genetically related and highlight the chemical dynamics of the mineralising system. In the following discussion, we argue that the mineralisation at Lienzer Schlossberg is part of the magmatic-hy-

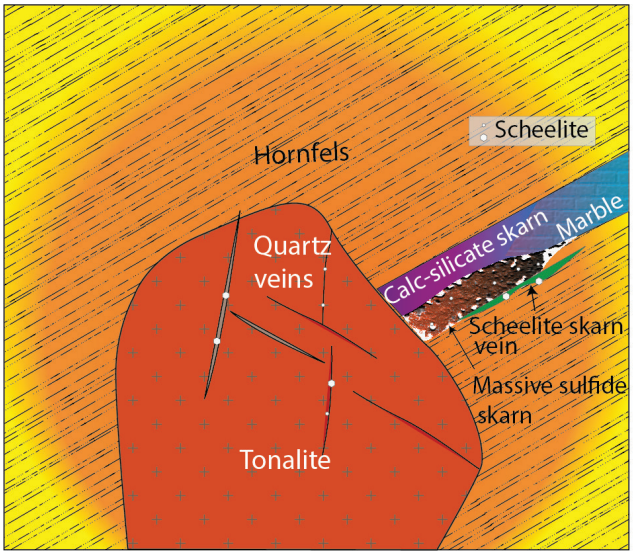

Figure 14: Schematic sketch illustrating the different mineralisation styles at area Schlossberg with scheelite; not to scale.

Analysis	SB16a-13	SB16a-15	SB14B	SB14B	SB14B	SB14I	SB14I	SB14F
mass%	An3	An8	An18	An25	An59	An37	An78	An111
SiO_2	51.88	51.73	49.28	49.34	50.27	51.85	51.08	51.71
TiO_2	0.04	0.01	0.00	0.01	0.00	0.01	0.00	0.16
Al_2O_3	0.27	0.23	0.18	0.15	0.20	0.31	0.13	1.42
FeO(T)	13.56	16.34	25.13	25.81	24.51	13.71	15.30	11.78
MnO	0.54	0.92	1.16	1.03	1.10	0.37	0.57	0.58
MgO	8.99	7.21	1.48	1.28	2.07	9.90	9.02	10.47
CaO	24.24	24.12	22.81	23.03	22.69	24.49	24.10	23.90
Na_2O	0.08	0.04	0.03	0.04	0.09	0.05	0.01	0.12
K_2O	0.01	0.00	0.00	0.00	0.00	0.00	0.01	0.00
Total	99.62	100.59	100.08	100.70	100.93	100.69	100.22	100.15
Recalculated								
Fe_2O_3	0.00	0.00	0.00	0.01	0.00	0.22	0.66	0.00
FeO	13.56	16.34	25.13	25.80	24.51	13.51	14.70	11.78
Total	99.62	100.59	100.08	100.70	100.93	100.71	100.28	100.15
Cations based on 6 O								
Si	2.001	2.003	2.004	2.000	2.014	1.979	1.975	1.966
Al	0.000	0.000	0.000	0.000	0.000	0.014	0.006	0.034
Fe^{3+}	0.000	0.000	0.000	0.000	0.000	0.006	0.019	0.000
ΣT	2.001	2.003	2.004	2.000	2.014	2.000	2.000	2.000
Al	0.012	0.011	0.009	0.007	0.009	0.000	0.000	0.029
Ti	0.001	0.000	0.000	0.000	0.000	0.000	0.000	0.004
Mg	0.517	0.416	0.090	0.078	0.123	0.563	0.520	0.593
Fe^{2+}	0.437	0.529	0.855	0.874	0.821	0.431	0.475	0.373
Mn	0.018	0.030	0.040	0.035	0.037	0.005	0.005	0.000
ΣM1	0.985	0.986	0.993	0.995	0.991	1.000	1.000	1.000
Mg	0.000	0.000	0.000	0.000	0.000	0.000	0.000	0.000
Fe^{2+}	0.000	0.000	0.000	0.000	0.000	0.000	0.000	0.001
Mn	0.000	0.000	0.000	0.000	0.000	0.007	0.014	0.019
Ca	1.002	1.001	0.994	1.000	0.974	1.002	0.998	0.973
Na	0.006	0.003	0.002	0.003	0.007	0.003	0.000	0.009
K	0.000	0.000	0.000	0.000	0.000	0.000	0.000	0.000
ΣM2	1.008	1.003	0.996	1.003	0.980	1.012	1.013	1.003
Endmembers; mole%								
Enstatite	26.2	21.1	4.5	3.9	6.3	28.0	25.8	30.3
Ferrosilite	23.1	28.3	45.2	45.8	43.9	22.1	24.6	20.1
Wollastonite	50.8	50.6	50.2	50.3	49.8	49.9	49.6	49.7

SB16a massive sulphide ore, SB14B pyroxene hornfels, SB14I calc-silicate fels, SB14F altered tonalite

Table 2. Selected EPMA analyses of clinopyroxene.

drothermal system related with the Oligocene Lienz/Edenwald intrusion. A highly schematic model illustrating the possible relationships of the different mineralisation events is sketched in Figure 14.

Initial isochemical contact metamorphism caused formation of the contact metamorphic aureole and transforming the low- to medium grade regional metamorphic rocks of the Thurntaler and Defereggen Complex to metapelitic hornfels. Skarn formation includes a high-temperature stage of calc-silicate minerals followed by formation of the scheelite-bearing sulphide skarn. The high-temperature skarn assemblage is best seen in calc-silicate fels containing grossular-rich garnet, diopside-hedenbergite, calcic plagioclase, vesuvianite and wollastonite. Only traces of scheelite were found in this calc-silicate fels. Similar anhydrous skarn associations with garnet, garnet-clinopyroxene and with increasing distance from the contact to the marble pyroxene-vesuvianite-wollastonite were described from the Pine Creek tungsten skarn (Newberry, 1982). Garnet of this stage is grossular with minor andradite and very little sub-calcic garnet endmembers (Fig. 8a). Clinopyroxene of this stage is intermediate diopside-hedenbergite (Fig. 8b). Vesuvianite is also of interest as it contains up to 1.5 mass % of fluorine indicating that fluorine was an element present at this stage (Tab. 3).

Analysis	SB14I	SB14	SB14I	SB14I	SB14I	SB14I	SB14I
mass%	An201	An203	An206	AN213	An220	An223	An229
SiO_2	37.28	37.40	36.59	36.73	36.60	37.19	37.62
TiO_2	0.66	0.64	1.60	0.67	3.11	3.09	0.61
Al_2O_3	16.53	16.59	16.46	16.97	15.48	15.79	16.87
FeO(T)	4.68	4.51	4.47	4.36	4.26	3.60	4.52
MnO	0.05	0.13	0.08	0.06	0.08	0.06	0.09
MgO	2.07	1.98	1.85	1.66	1.69	1.77	2.00
CaO	36.33	36.22	36.39	36.42	35.25	35.88	35.73
Na_2O	0.00	0.02	0.00	0.01	0.03	0.10	0.00
K_2O	0.01	0.00	0.00	0.00	0.01	0.01	0.01
F	1.14	1.23	1.25	0.76	1.13	0.44	1.41
Cl	0.12	0.09	0.19	0.09	0.14	0.00	0.15
H_2O	2.53	2.49	2.44	2.69	2.49	2.90	2.40
(F+Cl)≡O	-0.51	-0.54	-0.57	-0.34	-0.51	-0.18	-0.63
Total	100.90	100.75	100.75	100.08	99.76	100.63	100.79
Formula based on 68 O plus 10 anions*							
Si	18.052	18.112	17.779	17.917	17.907	17.960	18.173
ΣZ	18.052	18.112	17.779	17.917	17.907	17.960	18.173
Ti	0.242	0.232	0.586	0.244	1.144	1.124	0.220
Al	9.434	9.466	9.424	9.754	8.926	8.983	9.606
Fe*	1.897	1.825	1.817	1.778	1.741	1.452	1.824
Mn	0.021	0.053	0.032	0.024	0.034	0.025	0.038
Mg	1.491	1.431	1.338	1.206	1.236	1.273	1.443
ΣY	13.085	13.006	13.196	13.006	13.080	12.857	13.131
Ca	18.847	18.792	18.947	19.033	18.481	18.561	18.494
Na	0.004	0.022	0.000	0.012	0.029	0.091	0.004
K	0.009	0.002	0.002	0.000	0.005	0.006	0.007
ΣX	18.859	18.816	18.949	19.045	18.515	18.657	18.505
O	68	68	68	68	68	68	68
F	1.743	1.887	1.919	1.177	1.741	0.669	2.159
Cl	0.098	0.076	0.159	0.071	0.119	0.001	0.122
OH	8.160	8.037	7.922	8.752	8.141	9.330	7.719
Total cations	50.00	49.93	49.92	49.97	49.50	49.47	49.81

*for formula calculation see text

Table 3. Selected EPMA analyses of vesuvianite.

The skarn rocks at Lienzer Schlossberg have comparable features to major tungsten skarns in the world: (1) an early stage is characterised by anhydrous minerals and overprinted by retrograde alteration and (2) skarns developed at a pluton contact with impure limestones although this is a rare lithology in the study area. The composition of garnet and clinopyroxene, presence of pyrrhotite as the predominant sulphide and the low Mo contents of scheelite support that it belongs to the reduced skarn type (Einaudi et al., 1981; Meinert, 1992; Miranda et al., 2022). The main skarn stage is overprinted by the massive sulphide skarn. In this stage, the pyrrhotite-rich ore with minor chalcopyrite formed. Disseminated scheelite clearly belongs to this paragenesis. EPMA analyses revealed that pyrrhotite is of the mixed 5C and 6C structural subtypes (Fig. 10a, b). The gangue minerals in the massive sulphides are calcic amphiboles (ferro actinolite, actinolite; plotting in the tremolite field in Fig. 9b, Tab. 4) and diopside-hedenbergite (Fig. 8b, Tab. 2), which support the skarn affinity of the ore. The presence of hydrous phases like amphiboles together with sulphides suggests that this is a retrograde skarn. Pyrrhotite as the main sulphide is found in several reduced tungsten skarns like Saulau or Los Santos; it is typical for the retrograde skarn stage (Sánchez et al., 2009; Poitrenaud et al., 2019).

Spatially, the massive sulphides are found next to altered plutonic rocks. The pyroxene-plagioclase fels at the contact could represent an endoskarn. In this rock, clinopyroxene is very Fe-rich, close to the hedenbergite endmember (Fig. 8b). The magmatic calcian plagioclase (bytownite, anorthite) in the tonalite is altered to more

Analysis	SB16a-13	SB16a-15	SB4a-14	SB4a-14	SB4a-14	SB4a-16	SB4a-16	SB4a-18
mass%	An6	An7	An1	An3	An4	An2	An3	An9
SiO_2	49.36	48.06	54.00	55.10	54.69	54.34	54.26	53.45
P_2O_5	0.03	0.05	0.05	bdl	bdl	0.047	0.051	0.02
TiO_2	0.13	0.13	0.17	0.13	0.25	0.24	0.27	0.23
Al_2O_3	4.56	5.06	3.33	1.85	3.17	2.74	2.76	4.32
MnO	0.83	0.70	0.16	0.21	0.15	0.24	0.15	0.19
FeO	23.60	23.62	8.83	8.92	8.55	9.79	8.47	8.46
MgO	7.09	6.08	17.75	17.80	17.67	17.16	18.15	17.40
CaO	11.18	11.89	12.95	13.41	13.37	12.90	13.04	13.14
Na_2O	0.16	0.43	0.24	0.10	0.21	0.20	0.22	0.36
K_2O	0.10	0.25	0.10	0.06	0.09	0.11	0.14	0.16
F	na	na	na	na	na	na	na	na
Cl	0.39	0.99	0.14	0.08	0.10	0.16	0.05	0.14
O=F,Cl (calc)	-0.09	-0.22	-0.03	-0.02	-0.02	-0.04	-0.01	-0.03
Initial Total	97.34	97.05	97.68	97.63	98.23	97.90	97.54	97.85
Recalculated								
FeO	23.28	23.62	8.16	8.92	8.55	9.42	7.93	8.46
Fe_2O_3	0.35	0.00	0.74	0.00	0.00	0.41	0.60	0.00
H_2O^+	1.86	1.68	2.09	2.10	2.11	2.07	2.11	2.09
Total	99.24	98.73	99.84	99.73	100.34	100.01	99.71	99.94
Formula assignments								
Si	7.549	7.464	7.635	7.807	7.691	7.705	7.671	7.558
P	0.004	0.007	0.006			0.006	0.006	0.002
Al	0.447	0.529	0.359	0.193	0.309	0.289	0.322	0.440
T subtotal	8.000	8.000	8.000	8.000	8.000	8.000	7.999	8.000
Ti	0.015	0.015	0.018	0.013	0.026	0.026	0.028	0.025
Al	0.375	0.397	0.196	0.116	0.217	0.169	0.137	0.281
Fe^{3+}	0.040		0.079			0.043	0.064	
Mn^{2+}		0.092	0.001	0.025	0.018	0.017	0.007	0.023
Fe^{2+}	2.953	3.068	0.965	1.057	1.006	1.117	0.938	1.001
Mg	1.617	1.408	3.741	3.759	3.703	3.628	3.825	3.668
C subtotal	5.000	4.980	5.000	4.970	4.970	5.000	4.999	4.998
Mn^{2+}	0.108		0.018			0.012	0.011	
Fe^{2+}	0.025							
Ca	1.832	1.978	1.962	2.000	2.000	1.960	1.976	1.991
Na	0.034	0.022	0.020			0.028	0.013	0.009
B subtotal	1.999	2.000	2.000	2.000	2.000	2.000	2.000	2.000
Ca				0.036	0.014			
Na	0.013	0.107	0.044	0.028	0.056	0.028	0.046	0.090
K	0.019	0.050	0.017	0.010	0.016	0.020	0.025	0.029
A subtotal	0.032	0.157	0.061	0.074	0.086	0.048	0.071	0.119
O (non-W)	22	22	22	22	22	22	22	22
OH	1.900	1.740	1.967	1.981	1.976	1.961	1.988	1.967
Cl	0.100	0.260	0.033	0.019	0.024	0.039	0.012	0.033
W subtotal	2.000	2.000	2.000	2.000	2.000	2.000	2.000	2.000
Sum T,C,B,A	15.03	15.14	15.06	15.04	15.06	15.05	15.07	15.12
Species	ferro-act.	ferro-act.	actinolite	actinolite	actinolite	actinolite	actinolite	actinolite

na = not analysed; ferro-act. = ferro-actinolite

Table 4. Selected EPMA analyses of amphiboles.

sodic plagioclase (andesine, labradorite; Fig. 8c). A second generation of biotite is also formed, resembling potassic biotite alteration.

Finally, the intrusive rocks in vicinity to the massive sulphide skarn are affected by structure-controlled sericite-chlorite-carbonate alteration (Fig. 5). The highest-grade scheelite mineralisation is observed in these structural zones at the contact of the massive sulphides and the hornfelsic host rocks, where a scheelite-rich sericite-calcite-chlorite rock is developed. From the mineral assemblage it is deduced that this mineralisation could be a lower-temperature expression of the mineralising

Analysis	SB16a-12	SB16a-12	SB4a-16	SB4a-17	SB4a-17	SB14F	SB14F	SB14F
mass%	An6	An7	An4	An4	An9	An9	An10	An24
SiO_2	45.74	45.58	45.26	46.58	45.73	59.84	46.58	56.50
Al_2O_3	34.35	35.25	34.70	34.47	34.53	25.12	35.04	28.55
FeO(T)	1.02	0.21	0.41	0.22	1.12	0.02	0.05	0.03
CaO	18.15	19.16	18.62	18.37	17.62	6.44	17.65	10.40
Na_2O	1.21	0.79	0.91	1.25	1.07	7.27	1.24	5.33
K_2O	0.03	0.01	0.02	0.05	0.04	0.20	0.03	0.16
Total	100.50	100.99	99.93	100.93	100.12	98.89	100.58	100.96
Recalculated								
Fe_2O_3	1.12	0.23	0.46	0.24	0.61	0.00	0.00	0.00
FeO	0.01	0.00	0.00	0.00	0.56	0.02	0.05	0.03
Total	100.62	101.02	100.01	100.95	100.29	98.89	100.58	100.97
Cations based on 8 O								
Si	2.101	2.083	2.090	2.126	2.105	2.687	2.126	2.512
Al	1.860	1.899	1.888	1.854	1.873	1.329	1.885	1.496
Fe^{3+}	0.039	0.008	0.016	0.008	0.021	0.000	0.000	0.000
Fe^{2+}	0.000	0.000	0.000	0.000	0.022	0.001	0.002	0.001
Ca	0.893	0.938	0.921	0.898	0.869	0.310	0.863	0.496
Na	0.108	0.070	0.081	0.111	0.095	0.633	0.109	0.459
K	0.002	0.001	0.001	0.003	0.002	0.012	0.002	0.009
ΣZ (Z=Si+Al+Fe^{3+})	4.000	3.990	3.993	3.988	4.000	4.016	4.011	4.009
ΣX (X=Ca+Na+K)	1.004	1.008	1.006	1.012	0.996	0.955	0.976	0.965
Total cations	5.004	4.998	5.000	5.000	4.996	4.971	4.987	4.973
Endmembers, mole %								
Orthoclase	0.2	0.1	0.1	0.3	0.3	1.2	0.2	0.9
Albite	10.8	6.9	8.1	11.0	9.9	66.3	11.2	47.7
Anorthite	89.1	93.0	91.8	88.8	89.9	32.5	88.6	51.4
X_{An}	0.89	0.93	0.92	0.89	0.90	0.32	0.89	0.51
Name	bytownite	anorthite	anorthite	bytownite	bytownite	andesine	bytownite	labradorite

Table 5. Selected EPMA analyses of plagioclase.

system, the alteration resembling phyllic (sericite-carbonate) alteration. The very similar micro-structure and REE patterns of this scheelite with that from the massive sulphide ore (Scheelite 2) points to a genetic relationship of the mineralisation styles.

Another expression of the magmatic-hydrothermal activity is scheelite in the quartz veinlets and joints in the tonalite. During cooling of the intrusion, a set of steep ENE-WSW striking joints developed (Fig. 6a–c). Their uniform orientation indicates formation in the regional stress regime during emplacement of the Edenwald intrusion along the Periadriatic Fault System. These joints acted as pathways for the hydrothermal fluids exsolved from the magma transporting tungsten and precipitating it as scheelite along these joints.

Rarely, thin quartz veins also developed in the intrusive rocks. These stockwork-like veinlets consist of scheelite and quartz surrounded by thin selvages of alkalifeldspar (Figs. 6b, 7a). In this potassic alteration zone, plagioclase is not stable anymore. This type of veining and alteration resembles potassic high-temperature alteration seen in porphyry systems. The presence of minor copper in the massive sulphide ores may point to a possible link to porphyry systems where skarns are not uncommon. However, porphyry Cu-Mo systems are typically oxidised, in contrast to the rather reduced nature of tungsten skarns.

8.3. Comparison with other scheelite deposits in the Alps

Following the discovery of the world-class Felbertal deposit, geochemical surveying of stream sediments and greenfield exploration led to the identification of numerous geochemical tungsten anomalies in stream sediments (Thalmann et al., 1989; Pirkl et al., 2015) and the discovery of many scheelite showings in the Eastern Alps (Neinavaie et al., 1985) (Fig. 1). About 100 scheelite occurrences are known in Austria, which are exclusively bound to the Upper Austroalpine and Subpenninic units in the Eastern Alps (Fig. 1; Weber and Lipiarski, 2020; Altenberger et al., 2021). Based on the geological context and ongoing studies of scheelite micro-textures and trace elements, three groups of tungsten mineralisation can be distinguished in the Eastern Alps: (1) Strata-bound scheelite mineralisation in metacarbonate rocks partly with magnesite (Tux-Lanersbach, Mallnock) without any link to granitic rocks (Raith et al., 1995; Altenberger et al., 2024); (2) scheelite in metamorphosed vein and stockwork deposits in metabasites/orthogneisses (Felbertal, e.g., Raith et al., 2018) and in W-(Sn) skarns (Messelingscharte, Ordosch et al., 2019) with a spatial and genetic link to (meta)granitoids; and (3) scheelite in metamorphic Au-W and polymetallic veins (e.g., Schellgaden, Wieser et al., 2010).

Scheelite findings in the Lienz area can be clearly as-

Analysis	SB4-A-1a	SB4a-9a	SB16-A-3a	SB16a-11a	Sch5-4a	87317-7a	Sch3-1a	Sch3-1a
mass %	An9	An7	An1	An9	An2	An3	An5	An6
Fe	60.81	62.10	60.69	60.81	61.20	61.10	60.62	60.26
Co	0.14	0.14	0.09	0.11	0.09	0.03	0.13	0.20
Ni	0.01	0.01	bdl	0.04	0.02	0.03	0.04	0.06
Cu	bdl	bdl	bdl	bdl	0.07	bdl	0.01	bdl
S	38.52	37.72	38.91	39.29	38.67	39.46	39.12	39.63
Total	99.48	99.97	99.69	100.25	100.06	100.62	99.91	100.14
sum atoms = 1								
Fe	0.475	0.485	0.472	0.470	0.475	0.470	0.470	0.465
Co	0.001	0.001	0.001	0.001	0.001	0.000	0.001	0.001
Ni	0.000	0.000	0.000	0.000	0.000	0.000	0.000	0.000
Cu	0.000	0.000	0.000	0.000	0.001	0.000	0.000	0.000
S	0.524	0.514	0.527	0.529	0.523	0.529	0.528	0.533
Fe/S (S=1)	0.906	0.945	0.896	0.889	0.909	0.889	0.890	0.873

bdl below limit of detection

Table 6. Selected EPMA analyses of pyrrhotite.

signed to the group of granite-related tungsten deposits. However, it is not the only type of scheelite mineralisation in East Tyrol. Scheelite has also been discovered in the metabasites of the Thurntaler Complex and in polymetallic As-rich sulphide deposits (Höll, 1971; Krol, 1974; Portugaller, 2010). Prior to discovery of the Felbertal deposit, scheelite mineralisation was explored for example at Tafinalpe south of Innervillgraten. The main differences of scheelite mineralisation are: (1) the lack of felsic intrusives, (2) scheelite-bearing units show a regional metamorphic overprint (typically, scheelite is found in deformed metamorphic quartz-carbonate veins/mobilisates) and (3) the mineralisation is either pure scheelite or associated with arsenopyrite. From field observations and the structural evolution, scheelite mineralisation in the Thurntaler Complex is clearly older than in the Lienz area.

This new interpretation disagrees with the genetic ideas suggested by Fuchs (1982). He argued for a pre-Variscan formation of scheelite based on (1) lacking contact to the tonalite and (2) the observation of high-temperature lamellas in chalcopyrite. Geological mapping confirmed that the skarn mineralisation is situated within the contact aureole of the Lienz/Edenwald intrusion and is spatially close to the intrusive contact (Raith, 1983; Linner et al., 2013). Temperatures of skarn formation were certainly high enough to stabilise high-temperature polymorphs of chalcopyrite. It remains, however, to be clarified whether tungsten derived from remobilisation of pre-existing scheelite and interaction of the magmatic fluids with the immediate host rocks as previously suggested (Fuchs, 1982).

Intrusion-related mineralisation is rare among the Periadriatic intrusions. Skarn deposits are known from the Traversella pluton in the central Alps in Northern Italy (Fig. 1). The skarn mineralisation there is also associated with a calc-alkaline Periadriatic intrusion dated at 28–31 Ma (von Blanckenburg et al., 1998). A magnesian skarn hosting a polymetallic Fe-Cu-W deposit is associated with a diorite intrusion (Dubru et al., 1988). The skarn is developed in the contact metamorphic aureole at the contact between the intrusion and the metamorphic rocks of the Sesia-Lanzo geological unit. The magnetite skarn contains minor scheelite, chalcopyrite and uraninite and was mined until 1971 (Baldassarre et al., 2024). Zoned exoskarns (pyroxene, andradite) developed due to infiltration of high-temperature fluids and reaction within and at the contact with dolomitic host rock and calcic hornfels. Like in other skarn deposits a primary (550–625 °C) and secondary mineralisation stage (300–525 °C) have been distinguished (Auwera and André, 1991). Scheelite coexists with magnetite and formed during the retrograde skarn stage together with hydrous silicates and the sulphides. Despite the similarity – both skarn systems are linked with Periadriatic intrusions of similar age – a main difference is that Traversella is primarily a polymetallic magnetite skarn; i.e., it represents an oxidised skarn developed in more magnesian host rocks.

8.4. Geodynamic setting of skarn formation

Tungsten skarns commonly develop around plutons that are formed in continental collision/subduction settings. The host plutons are felsic with ca. 70 mass % SiO_2 on average and the plutonic rocks derived from calc-alkaline magmas and are metaluminous to peraluminous (Meinert, 1992). The Edenwald intrusion is a composite intrusion ranging in composition from gabbrodiorite, diorite, tonalite, granodiorite to rare granite; i.e., SiO_2 values range from about 55 to 75 mass % (Hutter, 2022). The rocks are calcic to calc-alkaline and grade from metaluminous to peraluminous. Their chemical signature is comparable to subduction-related magmas, but it is clear from the geological setting and the Oligocene age

Analysis [µg/g]	SB36-12	SB36-15	SB-23-3	SB-23-6	SB19-1	SB19-6	SB19-8	SB17-2-8	SB17-2-9	SB17-2-10
Type	qz-veinlet	qz-veinlet	wallpaper	wallpaper	dissem.	dissem.	dissem.	SCC-vein	SCC-vein	SCC-vein
Scheelite	1a	1a	1b	1b	2a	2b	3	3	2b	2a
Na	150	257	382	247	298	155	4.07	3.63	29.3	95.5
Sr	110	107	94.9	88.4	58.4	63.6	32.6	37.6	38	39.8
Y	187	386	720	675	3196	1021	37.4	32.5	580	1287
Nb	60.6	303	196	238	462	114	4.96	6.37	39.3	106
Mo	1094	1135	1001	849	7.83	12.8	83.8	117.8	27.9	7.6
Ta	0.456	3.22	4.27	5.54	3.43	2.08	<0.00207	<0.00233	<0.00198	1.78
U	0.0379	0.114	0.618	0.311	0.0485	0.2	<0.00127	<0.00120	0.31	0.154
La	94.5	127	119	46.3	71.2	124	4.7	2.7	109	60.4
Ce	326	469	434	248	369	513	17.2	10.3	361	269
Pr	52.4	92.7	80.6	54.6	86	106	3.45	1.99	56.9	51.9
Nd	254	526	423	318	698	567	20.5	11.8	283	331
Sm	65.1	161	135	120	449	173	7.16	5.51	76.4	146
Eu	2.92	4.6	12.5	7.11	25.1	13.4	2.67	1.54	20.6	22.8
Gd	57.3	159	120	131	765	190.8	9.27	6.71	87.7	195
Tb	8.09	21.4	22.4	23.4	146	33.6	1.26	1.07	14.7	40.4
Dy	44	108	138	143	923	221	7.44	6.7	100	274
Ho	8.03	18.9	26.3	26.9	163	43.8	1.43	1.41	20.5	57.1
Er	20.8	42.6	78.3	68.7	382	120	3.89	3.34	60.1	142
Tm	2.66	4.63	10.4	8.39	40.8	16.1	0.471	0.339	8.31	17.6
Yb	14.8	22.2	60.4	42.4	208	92.7	2.73	1.61	51.7	104
Lu	1.74	2.41	6.54	5.34	22.7	11.3	0.385	0.168	7.1	13.6
ΣREE+Y	952	1759	1666	1244	4349	2226	82.5	55.1	1257	1724

Table 7. LA-ICP-MS trace element analyses of scheelite; selected analyses.

that the Edenwald intrusion is not related to the subduction stage of the Alpine orogeny. It is one of the smaller Periadriatic intrusions, which spread along the Periadriatic Fault System from Pohorje in the east to Traversella in the west with the larger intrusions being Rieserferner, Adamello and Bergell. They are accompanied by swarms of acidic as well as basic dykes (lamprophyres; Fig. 1).

Previous Nd-Sr-O isotope studies confirm that the magmas formed from the mixing of basaltic melts derived from partial melting of the subcontinental lithospheric mantle with melted or assimilated continental crust (von Blanckenburg et al., 1998). The amounts of assimilated crust were modelled at 20–70 % demanding temperatures of 800–1000 °C for melting of the lower crust. Thus, tonalites and granodiorites include a large proportion of melted lower crustal material. Four different geodynamic models of formation of these melts were discussed in the literature (von Blanckenburg et al., 1998): (1) subduction, (2) lithospheric extension, (3) convective removal of a thickened thermal boundary layer and (4) slab break-off. The slab break-off model best explains the linear arrangement and lateral extent of the intrusions along the Periadriatic Fault System and concurrent exhumation of high-pressure rocks (von Blanckenburg and Davies, 1995; von Blanckenburg et al., 1998).

The only radiometric data available for the Edenwald intrusion is a Rb-Sr isochron date of ca. 30 Ma (Pölland diorite, Borsi et al., 1978). It is comparable with the ages published for the Rieserferner pluton (30 Ma), Rensen (31–32 Ma), Bergell (30–32 Ma) and other Periadriatic intrusions (see compilations in von Blanckenburg et al., 1998; Rosenberg, 2004; Neubauer et al., 2018). Emplacement of these intrusions is syn-collisional and restricted to the Periadriatic Fault System, an orogen-parallel, crustal-scale mylonitic belt (Rosenberg, 2004). The Periadriatic Fault System postdates subduction of the Penninic ocean and nappe stacking and it is linked with continent-continent collision of the European with the Adriatic plate. It consists of a set of kinematically linked large-scale faults, displaying different kinematics, but alltogether accommodating dextral transpression (Rosenberg, 2004). Ascent of the melts from deeper source regions was controlled by the Periadriatic Fault System and coeval transpressive deformation facilitated extrusive emplacement of the magmas in the country rocks at higher crustal levels.

Formation of the W-mineralised high-temperature quartz veins and joint fillings in the Edenwald pluton is structurally controlled. The main mineralised structures are trending ENE-WSW (Fig. 6c). These brittle structures must have formed after solidification of the magma during cooling of the pluton under sub-solidus conditions and acted as fluid pathways for the mineralising fluids. How formation of these mineralised structures is related to the regional stress regime and deformation events in this segment of the Periadriatic Fault System remains to be clarified in future structural geological studies.

9. Conclusions

A regional tungsten anomaly is known from the area south to southwest of Lienz in East Tyrol that is part of the crystalline Austroalpine nappe complex of the Eastern Alps. It is spatially linked with the Lienz/Edenwald intrusion and its contact-metamorphic aureole. The intrusion

is one of the smaller Periadriatic (ca. 30 Ma) calc-alkaline plutons occurring along the Periadriatic Fault System. It represents a rare Periadriatic intrusion where magmatic-hydrothermal mineralisation including a skarn system has developed.

Scheelite occurs in quartz veinlets and joints within the porphyritic tonalitic to granodioritic host rocks and in exoskarns that developed at the contact of the intrusion with Ca-rich host rocks. The skarn system is characterised by a tungsten-poor primary anhydrous calc-silicate stage and a retrograde skarn stage; the latter includes the scheelite-bearing massive sulphide skarn and scheelite-rich skarn veins. The ore stages, the mineral paragenesis and mineral compositions are comparable to reduced tungsten skarns, which notably have the highest economic potential of tungsten deposits.

Micro-textures and trace element systematics allow to distinguish several types of scheelite (i.e., Scheelite 1–3) that record the evolution of the hydrothermal fluids. Reduced conditions of ore fluids are indicated by the Fe^{3+}-poor compositions of garnet and clinopyroxene, the pyrrhotite-dominated sulphide assemblage and the low Mo content combined with the strongly negative Eu anomalies of scheelite. Scheelite evolved to more oxidising conditions with time as recorded by the trace elements. Among the dozens of scheelite showings known in different geological units in the Eastern Alps, those in the Lienz area are a unique example of a non-metamorphosed intrusion-related tungsten skarn system associated with a Cenozoic pluton of the Periadriatic Fault System.

Acknowledgements

This publication is largely based on the F. Hutter's master thesis carried out at Montanuniversität Leoben (Hutter, 2022). The presented trace element data of scheelite are an integral part of F. Altenberger's ongoing PhD thesis. Both theses are part of the W Alps project (see below). M. Zimmermann is thanked for sample preparation. F. Zaccarini for assistance with electron probe microanalysis. H. Paulick from GeoSphere Austria is thanked for administrative project support and his scientific input as mentor of F. Altenberger's PhD thesis. The W Alps project was funded through the Forschungspartnerschaft: Grundlagenorientierte Mineralrohstoffforschung (MRI) project scheme of GeoSphere Austria, financed by the former Federal Ministry of Agriculture, Regions and Tourism (Austria). Co-funding was provided by Wolfram Berg- und Hütten AG. S. Schmidt and K. Aupers are thanked for enabling this financial support and their scientific input. K. Bachmann is thanked for MLA analyses at Helmholtz Institute Freiberg. Constructive reviews by B. Schulz (Freiberg) und C. Patten (Innsbruck) are gratefully acknowledged. Finally, B. Joachim-Mrosko and K. Stüwe are thanked for their efficient and careful editorial handling of the manuscript.

References

Altenberger F., Raith J.G., Weilbold J., Auer C., Knoll T., Paulick H., Schedl A., Aupers K., Schmidt S., Neinavaie H., 2021. Casting new light on tungsten deposits in the Eastern Alps. Zeitschrift der Deutschen Gesellschaft für Geowissenschaften, 172/1, 63–72. https://doi.org/10.1127/zdgg/2021/0262.

Altenberger F., Auer T., Krause J., Auer A., Berndt J., 2023. G.O.Joe: A new non-commercial software tool for the processing of LA-ICP-MS data [Poster]: MinWien2023: Joint meeting of the Mineralogical Societies of Austria, Germany, and Slovakia, 17–21 September, University of Vienna, Austria. Available online at https://www.gojoe.software/.

Altenberger F., Krause J., Wintzer N.E., Iglseder C., Berndt J., Bachmann K., Raith J.G., 2024. Polyphase stratabound scheelite-ferberite mineralization at Mallnock, Eastern Alps, Austria. Mineralium Deposita. https://doi.org/10.1007/s00126-024-01250-x.

Auer C., 2016. 1971) Anglesit, Aktinolith, Anorthit, „Apatit", Allanit-(Ce), Kassiterit, Elektrum, Ilmenit, Monazit-(Ce), Hedleyit, Segnitit, Titanit, Wismut ged. und Zirkon als Neufunde vom Lienzer Schlossberg. In: Walter F., Auer C., Bernhard F., Hans-Peter Bojar F.B., Habel M., Hollerer C. E., Kolitsch U., Lamatsch P., Leikauf B., Löffler E., Niedermayr G., Postl W., Putz H., Reicht M., Schachinger T., Schillhammer H., Taucher J. (eds.), Neue Mineralfunde aus Österreich LXV, Carinthia II, 203/250, 217–218.

Auer C., 2022. 2239) Allanit-(Ce), ein Amphibolgruppenmineral, Chalkopyrit, Cobaltit, Fluorapatit, Galenit, Ilmenit, Löllingit, Molybdänit, Muskovit, Monazit-(Ce), Pyrrhotin, Rutil, Sphalerit, Xenotim-(Y) und Zirkon vom kleinen Pyrit-Arsenopyritschurf unweit des Hochsteinhauses, Lienzer Schloßberg, Osttirol. In: Walter F., Auer C., Berger F., Bernhard F., Bieler H., Bojar H.-P., Eck H., Jakely D., Kiseljak R., Knobloch E., Knobloch G., Kolitsch U., Krüger B., Löffler E., Postl W., Rausch L., Schachinger T., Schillhammer H., Schreieck E., Steck C., Števko M., Tropper P., (eds.), Neue Mineralfunde aus Österreich LXXI. Carinthia II, 212./132, 221–308.

Auwera J., André L., 1991. Trace elements (REE) and isotopes (O, C, Sr) to characterize the metasomatic fluid sources: evidence from the skarn deposit (Fe, W, Cu) of Traversella (Ivrea, Italy). Contributions to Mineralogy and Petrology, 106, 325–339. https://doi.org/10.1007/BF00324561.

Baldassarre G., Fiorucci A., Marini P., 2024. Recovery of critical raw materials from abandoned mine wastes: some potential case studies in northwest Italy. Materials Proceedings, 2023, 15, 77. https://doi.org/10.3390/materproc2023015077.

Bau M., 1991. Rare-earth element mobility during hydrothermal and metamorphic fluid-rock interaction and the significance of the oxidation state of europium. Chemical Geology, 93/3, 219–230. https://doi.org/10.1016/0009-2541(91)90115-8.

Becker M., de Villiers J., Bradshaw D., 2010. The mineralogy and crystallography of pyrrhotite from selected nickel and PGE ore deposits. Economic Geology, 105/5, 1025–1037. https://doi.org/10.2113/econgeo.105.5.1025.

Borsi S., Del Moro A., Sassi F.P., 1973. Metamorphic evolution of the Austridic rocks to the south of the Tauern Window (Eastern Alps): Radiometric and geo-petrologic data. Memorie della Societa Geologica Italiana, 12/4, 549–571.

Borsi S., Del Moro A., Sassi F.P., Zanferrari A., Zirpol G., 1978. New geopetrologic and radiometric data on the alpine history of the Austridic continental margin south of the Tauern Window (Eastern Alps). Memorie di scienze geologiche, 32, 1–17.

Brigo L., Omenetto P., 1983. Scheelite-bearing occurrences in the Italian Alps: Geotectonic and lithostratigraphic setting. In: Schneider H.-J., (ed.), Mineral deposits of the Alps and of the Alpine epoch in Europe, Special Publication Society for Geology Applied to Mineral Deposits. Springer, Berlin, Heidelberg, 3, 41–50. https://doi.org/10.1007/978-3-642-68988-8_5

Brugger J., Etschmann B., Pownceby M., Liu W., Grundler P., Brewe D., 2008. Oxidation state of europium in scheelite: Tracking fluid-rock interaction in gold deposits. Chemical Geology, 257, 26–33. https://doi.org/10.1016/j.chemeo.2008.08.003.

de Villiers J.P.R., Liles D.C., Becker M., 2009. The crystal structure of a naturally occurring 5C pyrrhotite from Sudbury, its chemistry, and vacancy distribution. American Mineralogist, 94, 1405–1410. ISSN: 0003-004X, 1410. https://doi.org/10.2138/am.2009.3081.

Dubru M., Auwera J.V., van Marcke de Lummen G., Verkaeren J., 1988. Distribution of scheelite in magnesian skarns at Traversella (Piemontese Alps, Italy) and Costabonne (Eastern Pyrenees, France): Nature of the associated magmatism and influence of fluid composition. In: Boissonnas J., Omenetto P., (eds.), Mineral deposits within the European Community. Springer Berlin Heidelberg, Berlin, Heidelberg, 117–134.

Eichhorn R., Höll R., Jagoutz E., Schärer U., 1997. Dating scheelite stages: A strontium, neodymium, lead approach from the Felbertal tungsten deposit, Central Alps, Austria. Geochimica et Cosmochimica Acta, 61/23, 5005–5022.

Einaudi M.T., Meinert L.D., Newberry R.J., 1981. A special issue devoted to skarn deposits. Introduction – terminology, classification, and composition of skarn deposits. Economic Geology, Seventy-fifth anniversary volume, 1905–1980, 77, 317–391.

Evans H.T., 1970. Lunar troilite: crystallography. Science, 167, 3918, 621–623. https://doi.org/DOI: 10.1126/science.167.3918.621.

Exel R., 1986. Erläuterungen zur Lagerstättenkarte von Osttirol. Archiv für Lagerstättenforschung der Geologischen Bundesanstalt, 7, 19–31.

Friedrich O.M., 1949. Erzmikroskopische Untersuchungen an Kärntner Lagerstätten III. Der Karinthin, 6, 102–105.

Fuchs H.W., 1982. Magnetkies- und Scheelitanreicherungen in den „Alten Gneisen" des Lienzer Schlossberges (Osttirol). Archiv für Lagerstättenforschung der Geologischen Bundesanstalt, 2, 67–70.

Furlani M., 1912. Der Drauzug im Hochpustertal. Mitteilungen der Geologischen Gesellschaft in Wien, 5, 252–271.

Ghaderi M., Palin M., Campbell I.H., Sylvester P.J., 1999. Rare earth element systematics in scheelite from hydrothermal gold deposits in the Kalgoorlie-Norseman Region, Western Australia. Economic Geology, 94, 423–438. https://doi.org/10.2113/gsecongeo.94.3.423.

Green C.J., Lederer G.W., Parks H.L., Zientek M.L., 2020. Grade and tonnage model for tungsten skarn deposits – 2020 update, Scientific Investigations Report: Reston, VA, p. 23.

Groat L., Hawthorne F., Ercit T.S., 1992. The chemistry of vesuvianite. Canadian Mineralogist, 30, 19–48.

Guhl M., Troll G., 1987. Die Permotrias von Kalkstein im Altkristallin der südlichen Deferegger Alpen (Österreich). Jahrbuch der Geologischen Bundesanstalt, 130/1, 37–60.

Haupt C.P., Krause J., Schulz B., Götze J., Chischi J., Berndt J., Klemme S., Schmidt S., Aupers K., Reinhardt N., 2024. New insights on the formation of the polymetamorphic Felbertal tungsten deposit (Austria, Eastern Alps) revealed by CL, EPMA, and LA-ICP-MS investigation, Mineralium Deposita. https://doi.org/10.1007/s00126-024-01284-1.

Hausberger G., Polegeg S., Pucher M., Punzengruber K., Thalmann F., 1982. Regionale Scheelitprospektion in Osttirol (Probenahme und erste Ergebnisse). Archiv für Lagerstättenforschung der Geologischen Bundesanstalt, 1, 53–60.

Hawthorne F.C., Oberti R., Harlow G.E., Maresch W.V., Martin R.F., Schumacher J.C., Welch M.D., 2012. Nomenclature of the amphibole supergroup. American Mineralogist, 97/11–12, 2031–2048. https://doi.org/10.2138/am.2012.4276.

Heinisch H., Schmidt K., 1976. Zur kaledonischen Orogenese in den Ostalpen. Geologische Rundschau, 65, 459–482.

Heinisch H., Schmidt K., 1984. Zur Geologie des Thurntaler Quarzphyllits und des Altkristallins südlich des Tauernfensters (Ostalpen, Südtirol). Geologische Rundschau, 73/1, 113–129. https://doi.org/10.1007/BF01820363.

Höll R., 1971. Scheelitvorkommen in Österreich. Erzmetall, 24/6, 273–282.

Höll R., 1979. Time- and stratabound early Paleozoic scheelite, stibnite and cinnabar deposits in the Eastern Alps. Verhandlungen der Geologischen Bundesanstalt, 1978/3, 369–387.

Hsu L.C., 1977. Effects of oxygen and sulfur fugacities on the scheelite-tungstenite and powellite-molybdenite stability relations. Economic Geology, 72/4, 664–670. https://doi.org/10.2113/gsecongeo.72.4.664.

Hutter F., 2022. Wolframvererzungen und Intrusionsgesteine am Lienzer Schlossberg, Osttirol. Master's thesis, Montanuniversität Leoben, Leoben, 200 pp. https://pureadmin.unileoben.ac.at/ws/portalfiles/portal/9334828/AC16582762.pdf.

Jensen K.R., Campos E., Wilkinson J.J., Wilkinson C.C., Kearsley A., Miranda-Díaz G., Véliz W., 2022. Hydrothermal fluid evolution in the Escondida porphyry copper deposit, northern Chile: evidence from SEM-CL imaging of quartz veins and LA-ICP-MS of fluid inclusions. Mineralium Deposita, 57/2, 279–300. https://doi.org/10.1007/s00126-021-01058-z.

Jochum K.P., Nohl U., Herwig K., Lammel E., Stoll B., Hofmann A.W., 2005. GeoReM: A new geochemical database for reference materials and isotopic standards. Geostandards and Geoanalytical Research, 29/3, 333–338. https://doi.org/10.1111/j.1751-908X.2005.tb00904.x.

Jochum K.P., Weis U., Stoll B., Kuzmin D., Yang Q., Raczek I., Jacob D.E., Stracke A., Birbaum K., Frick D.A., Günther D., Enzweiler J., 2011. Determination of reference values for NIST SRM 610–617 glasses following ISO guidelines. Geostandards and Geoanalytical Research, 35/4, 397–429. https://doi.org/10.1111/j.1751-908X.2011.00120.x.

Kelly D.P., Vaughan D.J., 1983. Pyrrhotine-pentlandite ore textures: a mechanistic approach. Mineralogical Magazine, 3, 237–253, 47/345, 453–463. https://doi.org/10.1180/minmag.1983.047.345.06.

Krol W., 1974. Geologisch-lagerstättenkundliche Untersuchungen im Gebiet nördlich von Sillian (Osttirol/Österreich). PhD thesis, University of Munich, 79 pp.

Linner M., 2003. Bericht 2002 über geologische Aufnahmen in den Deferegger Alpen auf Blatt 179 Lienz. Jahrbuch der Geologischen Bundesanstalt, 143/3, 493–502.

Linner M., Reitner J.M., Pavlik W., 2013. Geologische Karte 1:50 000, Blatt Lienz: Wien, Geologische Bundesanstalt.

Locock A.J., 2008. An Excel spreadsheet to recast analyses of garnet into end-member components, and a synopsis of the crystal chemistry of natural silicate garnets. Computers & Geosciences, 34/ISSN: 0098-3004, 1780. https://doi.org/10.1016/j.cageo.2007.12.013.

Locock A.J., 2014. An Excel spreadsheet to classify chemical analyses of amphiboles following the IMA 2012 recommendations. Computers & Geosciences, 62/ISSN: 0098-3004, 11. https://doi.org/10.1016/j.cageo.2013.09.011.

Meinert L.D., 1992. Skarns and skarn deposits. Geoscience Canada, 19/4, 145–162.

Miranda, A.C.R., Beaudoin G., Rottier B., 2022. Scheelite chemistry from skarn systems: implications for ore-forming processes and mineral exploration. Mineralium Deposita, 57:1469–1497. https://doi.org/10.1007/s00126-022-01118-y.

Nassau K., Loiacono G.M., 1963. Calcium tungstate – III: Trivalent rare earth substitution. Journal of Physics and Chemistry of Solids, 24/12, 1503–1510. https://doi.org/https://doi.org/10.1016/0022-3697(63)90090-8.

Neinavaie H., Pfeffer W., Thalmann F., 1985. Ergebnisse der geochemischen Prospektion auf Stahlveredler im Bundesgebiet. Berg- und Hüttenmännische Monatshefte, 130/4, 111–116.

Neinavaie M.H., 1979. Schichtengebundene Metallanreicherungen in den Schieferhüllen und in der Matreier Zone Ostirols, Ph.D. thesis, University of Innsbruck, 148 pp. https://bibsearch.uibk.ac.at/AC00905216

Neinavaie M.H., Ghassemi B., Fuchs H.W., 1983. Die Erzvorkommen Osttirols. Veröffentlichungen des Tiroler Landesmuseums Ferdinandeum, 63, 69–113.

Neubauer F., Heberer B., Dunkl I., Liu X., Bernroider M., Dong Y., 2018. The Oligocene Reifnitz tonalite (Austria) and its host rocks: Implications for Cretaceous and Oligocene-Neogene tectonics of the south-eastern Eastern Alps. Geologica Carpathica, 69. https://doi.org/10.1515/geoca-2018-0014.

Neubauer F., Sassi F.P., 1993. The Austro-Alpine quartzphyllites and related Palaeozoic formations. In: von Raumer J.F., and Neubauer F., (eds.), Pre-Mesozoic geology in the Alps. Springer, Berlin, Heidelberg, 423–439.

Newberry R.J., 1982. Tungsten-bearing skarns of the Sierra Nevada; I. The Pine Creek Mine, California. Economic Geology, 77/4, 823–844. https://doi.org/10.2113/gsecongeo.77.4.823.

Newberry R.J., Einaudi M.T., 1981. Tectonic and geochemical setting of tungsten skarn mineralization in the Cordillera. In: Dickinson W.R., Payne W.D., (eds.), Relations of tectonics to ore deposits in the southern Cordillera. 14. Arizona Geological Society Digest, 99–111.

Ordosch A., Raith J.G., Schmidt S., Aupers K., 2019. Polyphase scheelite and stanniferous silicates in a W-(Sn) skarn close to Felbertal tungsten mine, Eastern Alps. Mineralogy and Petrology, 113, 703–725. https://doi.org/10.1007/s00710-019-00675-x

Pettke T., Oberli F., Audétat A., Guillong M., Simon A.C., Hanley J.J., Klemm L.M., 2012. Recent developments in element concentration and isotope ratio analysis of individual fluid inclusions by laser ablation single and multiple collector ICP-MS. Ore Geology Reviews, 44, 10–38. https://doi.org/http://dx.doi.org/10.1016/j.oregeorev.2011.11.001

Pirkl H., Schedl A., Pfleiderer S., Neinanveie H., Reitner, H., Klein P., Hobiger G., Filzmoser P., Lipiarski P., Linner M., 2015. Geochemischer Atlas von Österreich – Bundesweite Bach- und Flusssedimentgeochemie (1978–2010). Geologische Bundesanstalt, Wien, 288 pp.

Poitrenaud T., Poujol M., Augier R., Marcoux E., 2019. The polyphase evolution of a late Variscan W/Au deposit (Salau, French Pyrenees): insights from REE and U/Pb LA-ICP-MS analyses. Mineralium Deposita, 55/6, 1127–1147. https://doi.org/10.1007/s00126-019-00923-2

Portugaller T., 2010. Scheelitvererzungen im Thurntaler Quarzphyllitkomplex, Osttirol: Petrographische und chemische Untersuchungen an Nebengesteinen und Bachsedimenten. Masterarbeit, Montanuniversität Leoben, Leoben, 190 pp.

Poulin R.S., Kontak D.J., McDonald A., McClenaghan M.B., 2018. Assessing scheelite as an ore-deposit discriminator using its trace-element and REE chemistry. The Canadian Mineralogist, 56/3, 265–302. https://doi.org/10.3749/canmin.1800005

Poulin R.S., McDonald A.M., Kontak D.J., McClenaghan M.B., 2016. On the relationship between cathodoluminescence and the chemical composition of scheelite from geologically diverse ore-deposit environments. The Canadian Mineralogist, 54/5, 1147–1173. https://doi.org/10.3749/canmin.1500023

Putnis A., 2002. Mineral replacement reactions: from macroscopic observations to microscopic mechanisms. Mineralogical Magazine, 66, 689–708.

Raimbault L., Baumer A., Dubru M., Benkerrou C., Croze V., Zahm A., 1993. REE fractionation between scheelite and apatite in hydrothermal conditions. American Mineralogist, 78/11–12, 1275–1285.

Raith J.G., 1983. Geologische Bearbeitung neugefundener Scheelitvererzungen in den Ostalpen, unpublished report: Eisenerz, Voest-Alpine AG, p. 39.

Raith J.G., Grum W., Prochaska W., Frank W., 1995. Polymetamorphism and polyphase deformation of the strata-bound magnesite-scheelite deposit, Tux-Lanersbach, eastern Alps, Austria. Economic Geology, 90/4, 763–781.

Raith J.G., Schmidt S., Aupers K., 2018. Field Trip Pre-EX-5. Tungsten deposit Felbertal, Salzburg, Austria. Berichte der Geologischen Bundesanstalt, 126, 7–46.

Ramdohr P., 1975. Die Erzmineralien und ihre Verwachsungen. 4. Auflage. Akademie-Verlag, Berlin, 1277 pp.

Rosenberg C.L., 2004. Shear zones and magma ascent; a model based on a review of the Tertiary magmatism in the Alps. Tectonics, 23, TC3002, doi 10.1029/2003tc001526. https://doi.org/10.1029/2003tc001526.

Sánchez S.M.T., Benito M.C.M., Pérez M.L.C., 2009. Mineralogical and physiochemical evolution of the Los Santos scheelite skarn, Salamanca, NW Spain. Economic Geology, 104/7, 961–995. https://doi.org/10.2113/econgeo.104.7.961

Schmid S.M., Fügenschuh B., Kissling E., Schuster R., 2004. Tectonic map and overall architecture of the Alpine orogen. Eclogae Geologicae Helvetiae, 97/1, 93–117.

Schmid, S., 2012. From deposit to concentrate: The basics of tungsten mining, Part 1: Project generation and project development. ITIA Newsletter Tungsten, June 2012.

Schulz B., 1991. Deformation und Metamorphose im Thurntaler Komplex (Ostalpen). Jahrbuch der Geologischen Bundesanstalt Wien, 134/2, 369–391.

Schulz B., 1993. P-T-deformation paths of Variscan metamorphism in the Austroalpine basement: controls on geothermobarometry from microstructures in progressively deformed metapelites. Schweizerische Mineralogische und Petrographische Mitteilungen, 73, 301–318.

Schulz B., Bombach K., 2003. Single Zircon Pb-Pb geochronology of the Early-Palaeozoic magmatic evolution in the Austroalpine basement to the south of the Tauern Window. Jahrbuch der Geologischen Bundesanstalt Wien, 143/2, 303–321.

Schulz B., Bombach K., Pawlig S., Brätz H., 2004. Neoproterozoic to Early-Palaeozoic magmatic evolution in the Gondwana-derived Austroalpine basement to the south of the Tauern Window (Eastern Alps). International Journal of Earth Sciences, 93/5, 824–843. https://doi.org/10.1007/s00531-004-0421-8.

Schulz B., Klemd R., Brätz H., 2006. Host rock compositional controls on zircon trace element signatures in metabasites from the Austroalpine basement. Geochimica et Cosmochimica Acta 70:697-710. doi: 10.1016/j.gca.2005.10.001.

Schulz B., Steenken A., Siegesmund S., 2008. Geodynamic evolution of an Alpine terrane – the Austroalpine basement to the south of the Tauern Window as a part of the Adriatic Plate (eastern Alps). Geological Society, London, Special Publications, 298/1, 5–44. https://doi.org/10.1144/sp298.2.

Sciuba M., Beaudoin G., Grzela D., Makvandi S., 2020. Trace element composition of scheelite in orogenic gold deposits. Mineralium Deposita, 55/6, 1149–1172. https://doi.org/10.1007/s00126-019-00913-4.

Seedorff E., Dilles J.H., Proffett J.M, Jr., Einaudi M.T., Zuercher L., Stavast W.J.A., Johnson D.A., Barton M.D., 2005. Porphyry deposits; characteristics and origin of hypogene features. In: Hedenquist J.W., Thompson J.F.H., Goldfarb R.J., Richards J.P., (eds.), Economic Geology One Hundreth Anniversary Volume 1905–2005. Society of Economic Geologists, Littleton, CO, 251–298.

Senarclens-Grancy W., 1965. Zur Grundgebirgs- und Quartärgeologie der Deferegger Alpen und ihrer Umgebung. Verhandlungen der Geologischen Bundesanstalt: Sonderheft G, 116/2, 246–255.

Shore M., Fowler A.D., 1996. Oscillatory zoning in minerals; a common phenomenon. The Canadian Mineralogist, 34/6, 1111–1126.

Siegesmund S., Heinrichs T., Romer R.L., Doman D., 2007. Age constraints on the evolution of the Austroalpine basement to the south of the Tauern Window. International Journal of Earth Sciences, 96, 415–432.

Siegesmund S., Oriolo S., Heinrichs T., Basei M., Nolte N., Hüttenrauch F., Schulz B., 2018. Provenance of Austroalpine basement metasediments: Tightening up Early Palaeozoic connections between peri-Gondwanan domains of central Europe and northern Africa. – International Journal of Earth Sciences, 107, 2293–2315. https://doi.org/10.1007/s00531-018-1599-5.

Stegmüller G., 2022. Tectonic Data Analyzer, Universität Graz, http://iewarchiv.uni-graz.at/software/tda.

Sverjensky D.A., 1984. Europium redox equilibria in aqueous solution. Earth and Planetary Science Letters, 67/1, 70–78.

Thalmann F., Schermann O., Schroll E., Hausberger G., 1989. Geochemical atlas of the Republic of Austria 1:1,000.000: Bohemian Massif and central zone of the Eastern Alps (Stream sediments <80 mesh>): Vienna (Austria), Voest-Alpine AG, Bundesversuchs- und Forschungsanstalt Arsenal, Geologische Bundesanstalt, p. 36.

Tokonami M., Nishiguchi K., Morimoto N., 1972. Crystal structure of a monoclinic pyrrhotite (Fe_7S_8). American Mineralogist, 57/7–8, 1066–1080.

Villiers J.P.R. d., Liles D.C., 2010. The crystal-structure and vacancy distribution in 6C pyrrhotite. American Mineralogist, 95, 148–152.

Voest-Alpine AG, 1979. Bericht über die 1979 im Freischurfgebiet Schlossberg-Lienz durchgeführten Untersuchungsarbeiten, unpublished report: Eisenerz, Voest Alpine AG, p. 6.

von Blanckenburg F., Davies J.H., 1995. Slab breakoff – a model for syn-

collisional magmatism and tectonics in the Alps. Tectonics, 14/1, 120–131. https://doi.org/10.1029/94tc02051
von Blanckenburg F., Kagami H., Deutsch A., Oberli F., Meier M., Wiedenbeck M., Barth S., Fischer H., 1998. The origin of Alpine plutons along the Periadriatic Lineament. Schweizerische Mineralogische und Petrographische Mitteilungen, 78/1, 55–66.
von Raumer J.F., Bussy F., Schaltegger U., Schulz B., Stampfli G.M., 2013. Pre-Mesozoic Alpine basements – their place in the European Paleozoic framework. – Geological Society America Bulletin, 125, 89–108, DOI: 10.1130/B30654.1
Warr L.N., 2021. IMA-CNMNC approved mineral symbols. Mineralogical Magazine, 85/ISSN: 0026-461X, 320. https://doi.org/10.1180/mgm.2021.43
Weber L., Lipiarski P., 2020. IRIS Online. Interaktives Rohstoff Informations System. GeoSphere Austria, Vienna. https://www.geologie.ac.at/services/webapplikationen/iris-interaktives-rohstoffinformationssystem (Accessed on 17 February 2024).
Wieser B., Raith J.G., Thöni M., Cornell D.H., Stein H., Paar, W., 2010. In-situ trace element and ID-TIMS Sm-Nd analysis of scheelite and Re-Os dating of molybdenite at Schellgaden, a Au-(W) deposit in the Eastern Alps, Austria. Pangeo 2010 Abstracts, Journal of Alpine Geology, 52, 253–254.

Received: 6.3.2024
Accepted: 28.5.2024
Editorial Handling: Bastian Joachim-Mrosko